AIAA–2000–0337
An Overview of the NCC Spray/Monte-Carlo-PDF Computations

M.S. Raju
Dynacs Engineering Company, Inc.
Brook Park, OH

38th Aerospace Sciences Meeting & Exhibit
January 10–13, 2000 / Reno, NV

An Overview of the NCC Spray/Monte-Carlo-PDF Computations

M.S. Raju*
Dynacs Engineering Co., Inc., NASA Glenn Research Center
2001 Aerospace Parkway
Brook Park, Ohio-44142

1 ABSTRACT

This paper advances the state-of-the-art in spray computations with some of our recent contributions involving scalar Monte Carlo PDF (Probability Density Function), unstructured grids and parallel computing. It provides a complete overview of the scalar Monte Carlo PDF and Lagrangian spray computer codes developed for application with unstructured grids and parallel computing. Detailed comparisons for the case of a reacting non-swirling spray clearly highlight the important role that chemistry/turbulence interactions play in the modeling of reacting sprays. The results from the PDF and non-PDF methods were found to be markedly different and the PDF solution is closer to the reported experimental data. The PDF computations predict that some of the combustion occurs in a predominantly premixed-flame environment and the rest in a predominantly diffusion-flame environment. However, the non-PDF solution predicts wrongly for the combustion to occur in a vaporization-controlled regime. Near the premixed flame, the Monte Carlo particle temperature distribution shows two distinct peaks: one centered around the flame temperature and the other around the surrounding-gas temperature. Near the diffusion flame, the Monte Carlo particle temperature distribution shows a single peak. In both cases, the computed PDF's shape and strength are found to vary substantially depending upon the proximity to the flame surface. The results bring to the fore some of the deficiencies associated with the use of assumed-shape PDF methods in spray computations. Finally, we end the paper by demonstrating the computational viability of the present solution procedure for its use in 3D combustor calculations by summarizing the results of a 3D test case with periodic boundary conditions. For the 3D case, the parallel performance of all the three solvers (CFD, PDF, and spray) has been found to be good when the computations were performed on a 24-processor SGI Origin work-station.

2 NOMENCLATURE

A	pre-exponent of an Arrhenius reaction rate term
a	non-unity exponent of an Arrhenius reaction rate term
$\underline{a}_n$	outward area normal vector of the nth surface, m^2
B_k	Spalding transfer number
b	non-unity exponent of an Arrhenius reaction rate term
C_D	drag coefficient
C_p	specific heat, J/(kg K)
C_ϕ	a constant in Eq. (39)
c_n	convection/diffusion coefficient of the nth face, kg/s
D	turbulent diffusion coefficient, m^2/s
d	droplet diameter, m
E_a	activation energy of an Arrhenius reaction rate term
h	specific enthalpy, J/kg
J_i^α	diffusive mass flux vector, kg/ms
k	turbulence kinetic energy, m^2/s^2
l_k	latent heat of evaporation, J/kg
$l_{k,eff}$	effective latent heat of evaporation, J/kg (defined in Eq. (11))
M_i	molecular weight of ith species, kg/kg-mole
m_k	droplet vaporization rate, kg/s
m_{ko}	initial mass flow rate associated with kth droplet group, kg/s
N_{av}	number of time steps employed in the PDF time-averaging scheme

*Engineering Specialist, Associate fellow AIAA.

N_f	number of surfaces contained in a given computational cell
N_m	total number of Monte Carlo particles per grid cell
N_p	total number of computational cells
n_k	number of droplets in kth group
P	pressure, N/m^2
P_r	Prandtl number
p	joint scalar PDF
R_u	gas constant, J/(kg K)
Re	Reynolds number
r_k	droplet radius, m
r_{ko}	initial droplet radial location, m
s_k	droplet radius squared, r_k^2, m^2
s_{mlc}	liquid source contribution of the gas-phase continuity equation
s_{mle}	liquid source contribution of the gas-phase energy equation
s_{mlm}	liquid source contribution of the gas-phase momentum equations
s_{mls}	liquid source contribution of the gas-phase species equations
s_α	liquid source contribution of the α variable
T	temperature, K
t	time, s
u_i	ith velocity component, m/s
u_{ik}	ith velocity component of kth droplet group, m/s
V_c	volume of the computational cell, m^3
w_α	chemical reaction rate, 1/s
$\dot{w}_j$	gas-phase chemical reaction rate, 1/s
x_i	Cartesian coordinate in the ith direction, m
y_j	mass fraction of jth species
$\underline{x}$	spatial vector
χ	mole fraction
Δt	local time step used in the PDF computations, s
Δt_f	local time step in the flow solver, s
Δt_{gl}	global time step in the spray solver, s
Δt_{il}	fuel injection time step, s
Δt_{ml}	allowable time step in the spray solver, s
ΔV	computational cell volume, m^3
δ	Dirac-delta function
ϵ	rate of turbulence dissipation, m^2/s^3
ϵ_j	species mass fraction at the droplet surface
$\epsilon_{\alpha s}$	species mass fraction at the droplet surface
Γ_ϕ	turbulent diffusion coefficient, kg/ms
λ	thermal conductivity, J/(ms K)
μ	dynamic viscosity, kg/ms
ω	turbulence frequency, 1/s
ϕ	represents a set of scalars of the joint PDF
$\underline{\psi}$	independent composition space
ρ	density, kg/m^3
σ	dimensionality of $\underline{\psi}$-space
τ	stress tensor term, kg/ms^2
θ	void fraction

Subscripts

f	represents conditions associated with fuel
g	global or gas-phase
i	index for the coordinate or species components
j	index for the species component
k	droplet group or liquid-phase
l	liquid-phase
m	conditions associated with N_m
n	nth-face of the computational cell
o	initial conditions or oxidizer
p	conditions associated with the properties of a grid cell
s	represents conditions at the droplet surface or adjacent computational cell
t	conditions associated with time
α	index for the scalar component of the joint PDF equation
,	partial differentiation with respect to the variable followed by it

Superscripts

~	Favre averaging
-	time averaging or average based on the Monte Carlo particles present in a given cell
//	fluctuations

3 INTRODUCTION

Spray combustion is of interest in a wide-variety of applications: gas-turbine combustors, internal combustion engines (diesel and spark-ignition), liquid-rocket motors, and industrial furnaces. A large fraction of the world's energy needs are met by the combustion of the liquid fuels. Because of its abundant use, the need for developing better predictive tools for aiding in the design of ever more efficient, pollution-free, and stable combustion devices has received considerable attention.[1-10]

The physical modeling of turbulent spray flames requires consideration of various complex and rate-controlling processes associated with turbulent transport, mixing, and chemical kinetics, fluid-dynamic

characteristics of fuel injection and spray formation, transport and vaporization characteristics of individual droplets, and the interaction of turbulence with chemical kinetics, among others. The interaction of turbulence with chemical kinetics may occur over a wide-range of disparate time and length scales. Turbulence plays an important role in determining the rates of mass and heat transfer, chemical reactions, and liquid-phase evaporation in many practical combustion devices. The influence of turbulence in a gaseous diffusion flame manifests itself in several forms, ranging from the so-called wrinkled or stretched flamelets regime to the distributed combustion regime, depending upon how turbulence interacts with various flame scales.[11-12] Although most of the turbulent spray combustion models are based on either diffusion or premixed gaseous flame theories, combustion in a spray flame is more complex and seldom occurs in a single mode.

There are several approaches used in the study of turbulent spray flames.[1-10] El Banhawy and Whitelaw[2] in their study on the prediction of the local flow properties in a spray flame employed an assumed shape PDF model with values for its mean and variance obtained from the solution of additional transport equations. Raju and Sirignano[4] in their study on multicomponent spray computations in a swirl-stabilized center-body combustor employed the eddy break-up model of Spalding[13] to take some effect of turbulence on combustion. The eddy break-up model might be applicable in cases where chemical reaction rates are either very fast or slow compared with the turbulent time scales.

Most of the turbulence closure models for reactive flows have difficulty in treating nonlinear reaction rates.[11-12] The use of assumed shape PDF methods was found to provide reasonable predictions for pattern factors and NO_X emissions at the combustor exit.[14] However, their extension to multi-scalar chemistry becomes quite intractable. The solution procedure based on the modeled joint composition PDF transport equation has an advantage in that it treats the nonlinear reaction rates without any approximation. This approach holds the promise of modeling various important combustion phenomena relevant to practical combustion devices such as flame extinction and blow-off limits, and unburnt hydrocarbons (UHC), CO, and NO_X predictions.[11-12,14]

The success of any numerical tools used in the multidimensional combustor modeling depends not only on the modeling and numerical accuracy considerations but also depends on the computational efficiency considerations as determined by the computer memory and turnaround times afforded by the present-day computers. With the aim of developing an efficient solution procedure for use in multidimensional combustor modeling, we extended the scalar Monte Carlo PDF approach to the modeling of sprays with parallel computing in order to facilitate large-scale combustor applications.[7] In this approach, the mean gas-phase velocity and turbulence fields are determined from the solution of a conventional CFD method, the scalar fields of species and enthalpy from a modeled PDF transport equation using a Monte Carlo method, and a Lagrangian-based dilute spray model is used for the liquid-phase representation. The application of this method showed reasonable agreement when detailed comparisons were made for two different cases involving an open and a confined swirl-stabilized spray flames.[7]

It is well known that considerable effort usually goes into generating structured-grid meshes for gridding up practical combustor geometries which tend to be very complex in shape and configuration. The grid generation time could be reduced considerably by making use of existing automated unstructured grid generators.[15-18] With the aim of advancing the current multi-dimensional computational tools used in the design of advanced technology combustors, two new computer codes - LSPRAY[8] and EUPDF[19] - were developed here, thereby extending our previous work[7] on the Monte Carlo PDF and sprays to unstructured grids as a part of the National Combustion Code (NCC) activity. NCC is being developed in the form of a collaborative effort between NASA GRC, aircraft engine manufacturers, and several other government agencies and contractors.[17] The unstructured 3D solver is designed to be massively parallel and accommodates the use of an unstructured mesh with mixed elements comprising of either triangular, quadrilateral, and/or tetrahedral type. The ability to perform the computations on unstructured meshes allows representation of complex geometries with relative ease. The application of the unstructured grid extension to a confined swirl-stabilized spray flame provided reasonable agreement with the available droplet velocity measurements.[9]

A current status of the the use of the parallel computing in turbulent reacting flows involving sprays, scalar Monte Carlo PDF and unstructured grids was described in Ref. 10. It also outlines several numerical techniques developed for overcoming

some of the high computer time-and-storage limitations placed by the use of Monte Carlo solution methods. The parallel performance of both the PDF and CFD computations was found to be excellent but the results were mixed for the spray module showing reasonable performance on massively parallel computers like Cray T3D; but its performance was poor on the workstation clusters. In order to improve the parallel performance of the spray module, two different domain decomposition strategies were developed and the results from both strategies were summarized.[10]

The main objective of our present work is to to investigate the importance of considering chemistry/turbulence interactions in the calculation of a reacting spray. This was done by making detailed comparisons for the case of a reacting non-swirling spray for which experimental data was reported by McDonell and Samuelson.[20] The comparisons involved predictions from two different sets of computations, one in which the solution for the temperature and species fields is obtained from the use of the scalar Monte Carlo PDF method and in the other they are obtained from the solution of a conventional CFD solution. The second objective is to demonstrate the computational viability of the present solution procedure for its use in 3D computations. This was done by summarizing the results of a 3D test case which was designed primarily to examine the applicability of the spray particle search algorithm in 3D computations and of the newly-implemented periodic boundary conditions. For clarity, the overall solution procedure from Ref. 10 is repeated here. However, for a detailed account of the parallel performance together with the development and implementation of the parallel method, the interested reader is referred to Ref. 10.

First, complete details of the overall solution procedure with a particular emphasis on the PDF and spray algorithms are presented along with several other numerical issues related to the coupling between the CFD, spray, and PDF solvers. It is followed by the results-and-discussion section where the application of the method to predict the local properties of two different cases are presented. Finally, we conclude the paper by presenting a brief summary of important results along with the parallel performance of the three solvers (CFD, PDF, and spray).

4 GOVERNING EQUATIONS FOR THE GAS PHASE

Here, we summarize the conservation equations for the gas-phase in Eulerian coordinates derived for the multicontinua approach.[21] This is done for the purpose of identifying the interphase source terms arising from the exchanges of mass, momentum, and energy with the liquid-phase.

The conservation of the mass leads to:

$$[\bar{\rho}V_c]_{,t} + [\bar{\rho}V_c u_i]_{,x_i} = s_{mlc} = \sum_k n_k\, m_k \qquad (1)$$

For the conservation of the jth species, we have:

$$[\bar{\rho}V_c y_j]_{,t} + [\bar{\rho}V_c u_i y_j]_{,x_i} - [\bar{\rho}V_c D y_{j,x_i}]_{,x_i} - \bar{\rho}V_c \dot{w}_j =$$

$$s_{mls} = \sum_k \epsilon_j\, n_k\, m_k \qquad (2)$$

where

$$\sum_j \dot{w}_j = 0 \; and \; \sum_j \epsilon_j = 1$$

For the momentum conservation, we have:

$$[\bar{\rho}V_c u_i]_{,t} + [\bar{\rho}V_c u_i u_j]_{,x_j} + [pV_c]_{,x_i} -$$

$$[\theta V_c \tau_{ij}]_{,x_j} - [(1-\theta)V_c \tau_{ij}]_{,x_j} = s_{mlm} =$$

$$\sum_k n_k\, m_k\, u_{ki} - \sum_k \frac{4\pi}{3}\, \rho_k\, r_k^3\, n_k\, u_{ki,t} \qquad (3)$$

where θ = the void fraction of the gas which is defined as the ratio of the equivalent volume of gas to a given volume of a gas and liquid mixture. For dilute sprays, the void fraction is assumed to be equal to one. The shear stress τ_{ij} in Eq. (3) is given by:

$$\tau_{ij} = \mu[u_{i,x_j} + u_{j,x_i}] - \frac{2}{3}\delta_{ij} u_{i,x_j}$$

For the energy conservation, we have:

$$[\bar{\rho}V_c h]_{,t} + [\bar{\rho}V_c u_i h]_{,x_i} - [\theta V_c \lambda T_{,x_i}]_{,x_i} - [(1-\theta)V_c \lambda_l T_{,x_i}]_{,x_i}$$

$$- [\theta V_c p]_{,t} = s_{mle} = \sum_k n_k\, m_k \left(h_s - l_{k,eff}\right) \qquad (4)$$

5 GAS-PHASE SCALAR JOINT PDF EQUATION

The transport equation for the density-weighted joint PDF of the compositions, $\tilde{p}$, is:

$$
\begin{aligned}
&[\bar{\rho}\tilde{p}]_{,t} \quad + \quad [\bar{\rho}\tilde{u}_i\tilde{p}]_{,x_i} \\
&\{Transient\}\ \{Mean\ convection\} \\
&+ [\bar{\rho}w_\alpha(\underline{\psi})\tilde{p}]_{,\psi_\alpha} \ = \ -[\bar{\rho} < u_i'' \mid \underline{\psi} > \tilde{p}]_{,x_i} \\
&\{Chemical\ reactions\} \quad \{Turbulent\ convection\} \\
&- [\bar{\rho} < \frac{1}{\rho} J^\alpha_{i,x_i} \mid \underline{\psi} > \tilde{p}]_{,\psi_\alpha} - [\bar{\rho} < \frac{1}{\rho} s_\alpha \mid \underline{\psi} > \tilde{p}]_{,\psi_\alpha} \quad (5) \\
&\{Molecular\ mixing\} \quad \{Liquid\text{-}phase\ contribution\}
\end{aligned}
$$

where

w_α	=	chemical source term for the α-th composition variable,
$< u_i'' \mid \underline{\psi} >$	=	conditional average of Favre velocity fluctuations,
$< \frac{1}{\rho} J^\alpha_{i,x_i} \mid \underline{\psi} >$	=	conditional average of scalar dissipation, and
$< \frac{1}{\rho} s_\alpha \mid \underline{\psi} >$	=	conditional average of spray source terms.

The terms on the left-hand side of the above equation could be evaluated without any approximation, but the terms on the right-hand side of the equation require modeling. The first term on the right represents transport in physical space due to turbulent convection.[12] Since the joint PDF, $\tilde{p}$, contains no information on velocity, the conditional expectation of $< u_i'' \mid \underline{\psi} >$ needs to be modeled. It is modeled based on a gradient-diffusion model with information supplied on the turbulent flow field from the flow solver.[12]

$$
- < u_i'' \mid \underline{\psi} > \tilde{p} = \Gamma_\phi \tilde{p}_{,x_i} \qquad (6)
$$

The fact that the turbulent convection is modeled as a gradient-diffusion makes the turbulent model no better than the $k-\epsilon$ model. The uncertainties associated the use of a standard $k-\epsilon$ turbulence model to swirling flows are well known.[22] Some of the modeling uncertainties associated with the use of the standard $k-\epsilon$ model would be addressed in our future studies with the implementation of a non-linear $k-\epsilon$ developed for the modeling of swirling flows.[22]

The second term on the right-hand side represents transport in the scalar space due to molecular mixing. A mathematical description of the mixing process is rather complicated, and the interested reader is referred to Ref. 12. Molecular mixing is accounted for by making use of the relaxation to the ensemble mean submodel.[11]

$$
< \frac{1}{\rho} J^\alpha_{i,x_i} \mid \underline{\psi} > = -C_\phi \omega (\phi_\alpha - \bar{\phi}_\alpha) \qquad (7)
$$

where $\omega = \epsilon/k$, and C_ϕ is a constant. For a conserved scalar in a homogeneous turbulence, this model preserves the PDF shape during its decay, but there is no relaxation to a Gaussian distribution.[12] However, the results of Ref. 14 indicate that the choice between the different widely-used mixing models is not critical in the distributed reaction regime of premixed combustion as long as the turbulent mixing frequencies are above 1000 Hz. Most of the practical combustors seem to operate at in-flame mixing frequencies of 1000 Hz and above. The application of this mixing model seemed to provide some satisfactory results when applied to flows representative of those encountered in the gas-turbine combustion.[14]

The third term on the right-hand side represents the contribution from the spray source terms:

$$
< \frac{1}{\rho} s_\alpha \mid \underline{\psi} > = \frac{1}{\bar{\rho}\Delta V} \sum n_k m_k (\epsilon_{\alpha s} - \phi_\alpha) \qquad (8)
$$

where $\phi_\alpha = y_\alpha, \alpha = 1, 2, ..., s = \sigma - 1$

$$
< \frac{1}{\rho} s_\alpha \mid \underline{\psi} > = \frac{1}{\bar{\rho}\Delta V} \sum n_k m_k (-l_{k,eff} + h_{ks} - \phi_\alpha) \qquad (9)
$$

where $\phi_\sigma = h$ and is defined by:

$$
h \ = \ \sum_{i=1}^{\sigma-1} y_i h_i \qquad (10)
$$

where

$$
h_i = h^\circ_{fi} + \int_{T_{ref}}^{T} C_{pi} y_i dT,
$$

$$
C_{pi} = \frac{R_u}{W_i}(A_{1i} + A_{2i}T + A_{3i}T^2 + A_{4i}T^3 + A_{5i}T^4),
$$

h°_{fi} is the heat of formation of ith species, R_u is the universal gas constant, $\epsilon_{\alpha s}$ is a mass fraction of the

evaporating species at the droplet surface, and $l_{k,eff}$ is the effective latent heat of vaporization as modified by the heat loss to the droplet interior:

$$l_{k,eff} = l_k + 4\pi \frac{\lambda_l r_k^2}{m_k} \left(\frac{\partial T_k}{\partial r}\right)_s \tag{11}$$

Here we assumed that the spray source terms could be evaluated independent of the fluctuations in the gas-phase compositions of species and enthalpy. Eqs. (8)-(10) represent the modeled representation for the conditional averages of the spray contribution to the PDF transport equation.

6 LIQUID-PHASE EQUATIONS

The spray model is based on the multicontinua approach which allows for resolution on a scale greater than the average spacing between two neighboring droplets. A Lagrangian scheme is used for the liquid-phase equations as it eliminates errors associated with numerical diffusion. The vaporization model of a polydisperse spray takes into account the transient effects associated with the droplet internal heating, the forced convection effects associated with droplet internal circulation and the phenomena associated with boundary layers and wakes formed in the intermediate droplet Reynolds number range.[4] The present formulation is based on a deterministic particle-tracking method and on a dilute spray approximation which is applicable for flows where the droplet loading is low. Not considered in the present formulation are the effects associated with the droplet breakup, the droplet/shock interaction, the multi-component nature of liquid spray and the phenomena associated with dense spray effects and super-critical conditions. The spray method provided some favorable results when applied to several unsteady and steady-state calculations.[4-10]

For the particle position of the kth droplet group, we have:

$$\frac{dx_{ik}}{dt} = u_{ik} \tag{12}$$

For the droplet velocity:

$$\frac{du_{ik}}{dt} = \frac{3}{16} \frac{C_D \mu_{gs} Re_k}{\rho_k r_k^2} [u_{ig} - u_{ik}] \tag{13}$$

where

$$Re_k = 2\frac{r_k \rho_g}{\mu_{gs}} [(u_g - u_k) . (u_g - u_k)]^{1/2} \tag{14}$$

$$C_D = \frac{24}{Re_k} \left(1 + \frac{Re_k^{2/3}}{6}\right) \tag{15}$$

For droplet size, the droplet regression rate is determined from one of three different correlations depending upon the droplet-Reynolds-number range. When $Re_k > 20$, the regression rate is determined based on a gas-phase boundary-layer analysis valid for Reynolds numbers in the intermediate range.[23] The other two correlations, valid when $Re_k \leq 20$, are taken from Clift et al.[24]

$$\frac{ds_k}{dt} = -2\frac{\mu_l}{\rho_k} \left[\frac{2}{\pi} Re_k\right]^{1/2} f(B_k) \quad if\ Re_k > 20$$

$$\frac{ds_k}{dt} = -\frac{\mu_l}{\rho_k} \left[1 + (1 + Re_k)^{1/3}\right] Re_k^{0.077} ln(1 + B_k)$$

$$if\ 1 < Re_k \leq 20 \tag{16}$$

$$\frac{ds_k}{dt} = -\frac{\mu_l}{\rho_k} \left[1 + (1 + Re_k)^{1/3}\right] ln(1+B_k) \quad if\ \ Re_k < 1$$

where B_k is the Spalding transfer number defined in Eq. (22). The function $f(B_k)$ is obtained from the solution of Emmon's problem.[25] The range of validity of this function was extended in Raju and Sirignano[4] to consider the effects of droplet condensation.

The internal droplet temperature is determined based on a vortex model.[23] The governing equation for the internal droplet temperature is given by:

$$\frac{\partial T_k}{\partial t} = 17 \frac{\lambda_l}{C_{pl}\rho_l r_k^2} \left[\alpha \frac{\partial^2 T_k}{\partial \alpha^2} + (1 + C(t)\alpha) \frac{\partial T_k}{\partial \alpha}\right] \tag{17}$$

where

$$C(t) = \frac{3}{17} \left[\frac{C_{pl}\rho_l}{\lambda_l}\right] r_k \frac{dr_k}{dt} \tag{18}$$

where α represents the coordinate normal to the streamsurface of a Hill's Vortex in the circulating fluid, and $C(t)$ represents a nondimensional form of the droplet regression rate. The initial and boundary conditions for Eq. (17) are given by:

$$t = t_{injection}, \quad T_k = T_{k,o} \tag{19}$$

$$\alpha = 0, \quad \frac{\partial T_k}{\partial \alpha} = \frac{1}{17} \left[\frac{C_{pl}\rho_l}{\lambda_l}\right] r_k^2 \frac{\partial T_k}{\partial t} \tag{20}$$

$$\alpha = 1, \quad \frac{\partial T_k}{\partial \alpha} = -\frac{3}{32} \frac{\rho_k}{\lambda_l} \left[\frac{C_p(T_g - T_{ks})}{B_k} - l_k\right] \frac{ds_k}{dt} \tag{21}$$

where $\alpha = 0$ refers to the vortex center, and $\alpha = 1$ refers to the droplet surface.

The Spalding transfer number is given by:

$$B_k = \frac{C_p(T_g - T_{ks})}{l_{k,eff}} = \frac{(y_{fs} - y_f)}{(1 - y_{fs})} \tag{22}$$

$$y_{fs}^{-1} = 1 + \frac{M_a}{M_f}\left(\chi_{fs}^{-1} - 1\right) \tag{23}$$

where M_a is the molecular weight of the gas excluding fuel vapor.

Based on the assumption that phase equilibrium exists at the droplet surface, the Clausius-Clapeyron relationship yields

$$\chi_{fs} = \frac{P_n}{P} exp\left[\frac{l_k}{R_u}\left(\frac{1}{T_b} - \frac{1}{T_{ks}}\right)\right] \tag{24}$$

In Eq. (14), the molecular viscosity is evaluated at a reference temperature using Sutherland's equation

$$\mu_{gs}(T_{ref}) = 1.4637\ 10^{-6}\frac{T_{ref}^{3/2}}{T_{ref} + 120} \tag{25}$$

where

$$T_{ref} = \frac{1}{3}T_g + \frac{2}{3}T_{ks} \tag{26}$$

The droplets may evaporate, move along the wall surfaces, and/or reflect with reduced momentum upon droplet impingement with the combustor walls. In our present computations, subsequent to the droplet impingement with the walls, the droplets are assumed to flow along the wall surfaces with a velocity equal to that of the surrounding gas.

7 DETAILS OF DROPLET FUEL INJECTION

The success of any spray model depends a great deal on the specification of the appropriate injector exit conditions. However, a discussion involving the physics of liquid atomization is beyond the scope of this subject matter. In our present computations, the liquid fuel injection is simulated by introducing a discretized parcel of liquid mass in the form of spherical droplets at the beginning of every fuel-injection time step.

For certain cases, the fuel-injection time step, Δt_{il}, needs to be determined based on the resolution permitted by the length and time scales associated with several governing parameters such as average grid spacing and average droplet spacing and velocity. However, our experience showed that for the case of a steady-state solution, a time step based on the average droplet lifetime yields better convergence.[4-6] Its value typically ranges between 1 and 2 milli-seconds for the case of reacting flows.

The spray computations facilitate fuel injection through the use of a single fuel injector comprised of different holes.[5-6] However, multiple fuel injection in a steady-state calculation could be simulated by simply assigning different initial conditions for the spatial locations of the droplet groups associated with each one of the different holes. For a polydisperse spray, the spray computations require inputs for the number of droplet groups in a given stream and for the initial droplet locations and velocities. However, the number of droplets in a given group and their sizes could be either input directly or computed from a properly chosen function for the droplet size distribution. The specified initial inputs should be representative of the integrated averages of the experimental conditions.[5-10]

One correlation typical of those used for the droplet size distribution is taken from Ref. 2:

$$\frac{dn}{n} = 4.21\ 10^6\left[\frac{d}{d_{32}}\right]^{3.5} e^{-16.98\left(\frac{d}{d_{32}}\right)^{0.4}}\frac{dd}{d_{32}} \tag{27}$$

where n is the total number of droplets and dn is the number of droplets in the size range between d and $d + dd$. The Sauter mean diameter, d_{32}, could be either specified or estimated from the following correlation:[26]

$$d_{32} = B_d\frac{2\pi\sigma_l}{\rho_g V_T^2}\lambda_m^* \tag{28}$$

where B_d is a constant, V_T is the average relative velocity between the liquid interface and the ambient gas, and λ_m^* is a function of the Taylor number, $(\rho_l\sigma_l^2)/(\rho_g\mu_l^2 V_T^2)$.

A typical droplet size distribution obtained from the above correlation in terms of the cumulative percentage of droplet number and mass as a function of the droplet diameter is shown in Fig. 1.[7]

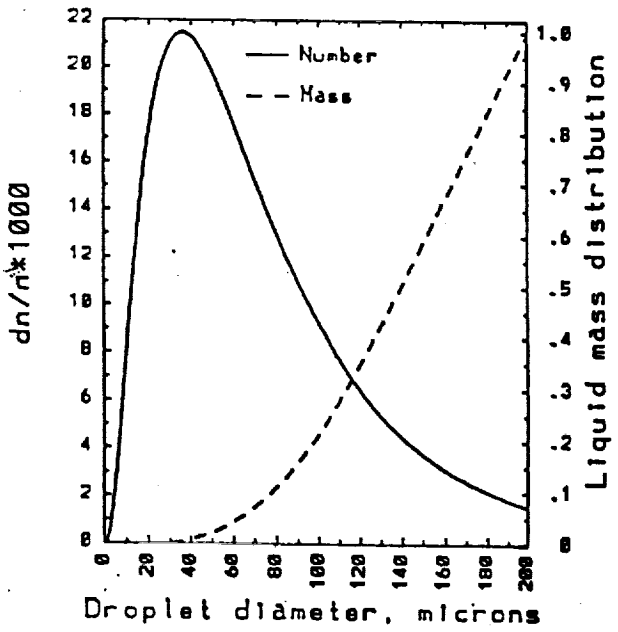

Figure 1 Droplet-size distribution.

8 CFD SOLUTION ALGORITHM

The gas-phase mass and momentum conservation equations together with the standard $k-\epsilon$ turbulence equations with wall functions are solved by making of a finite-volume solver with an explicit fourth-stage Runge-Kutta scheme. Further details of the code can be found in Refs. 16 & 18.

9 PDF SOLUTION ALGORITHM

In order to facilitate the integration of the Monte Carlo PDF method in a finite-volume context, the volume integrals of convection and diffusion in Eq. (5) were first recast into surface integrals by means of a Gauss's theorem.[27] Partial integration of the PDF transport equation would yield:

$$\tilde{p}_p(\underline{\psi}, t+\Delta t) = (1 - \frac{c_p \Delta t}{\bar{\rho}\Delta V})\tilde{p}_p(\underline{\psi}, t)$$

$$+ \sum_n \frac{c_n \Delta t}{\bar{\rho}\Delta V}\tilde{p}_n(\underline{\psi}, t) - \Delta t[w_\alpha(\underline{\psi})\tilde{p}]_{,\psi_\alpha}$$

$$- \Delta t[< \frac{1}{\rho} J^\alpha_{i,x_i} \mid \underline{\psi} > \tilde{p}]_{,\psi_\alpha} - \Delta t[< \frac{1}{\rho} s_\alpha \mid \underline{\psi} > \tilde{p}]_{,\psi_\alpha} \quad (29)$$

where subscript n refers to the nth-face of the computational cell. The coefficient c_n represents the transport by convection and diffusion through the nth-face of the computational cell, p. The convection/diffusion coefficients in the above equation are determined by one of the following two expressions:

$$c_n = \Gamma_\phi(\frac{2\underline{a}_n \cdot \underline{a}_n}{\Delta V_p + \Delta V_s}) + max[0, -\bar{\rho}\underline{a}_n \cdot \underline{u}_n]$$

$$c_n = max[|0.5\bar{\rho}\underline{a}_n \cdot \underline{u}_n|, \Gamma_\phi(\frac{2\underline{a}_n \cdot \underline{a}_n}{\Delta V_p + \Delta V_s})\,] - 0.5\bar{\rho}\underline{a}_n \cdot \underline{u}_n$$

and

$$c_p = \sum_n c_n$$

In both the above expressions for c_n, a cell-centered finite-volume derivative is used to describe the viscous fluxes; but an upwind differencing scheme is used for the convective fluxes in the first expression and a hybrid differencing scheme in the second.

9.1 Numerical Method Based on Approximate Factorization

The transport equation is solved by making use of an approximate factorization scheme.[12] Eq. (29) can be recast as:

$$\tilde{p}_p(\underline{\psi}, t+\Delta t) =$$

$$(I+\Delta tR)((I+\Delta tS)(I+\Delta tM)(I+\Delta tT)\tilde{p}_p(\underline{\psi}, t)+O(\Delta t^2) \quad (30)$$

where I represents the unity operator and T, M, S, and R denote the operators associated with spatial transport, molecular mixing, spray, and chemical reactions, respectively. The operator is further split into a sequence of intermediate steps:

$$\tilde{p}^\star_p(\underline{\psi}, t) = (I + \Delta tT)\tilde{p}_p(\underline{\psi}, t) \quad (31)$$

$$\tilde{p}^{\star\star}_p(\underline{\psi}, t) = (I + \Delta tM)\tilde{p}^\star_p(\underline{\psi}, t) \quad (32)$$

$$\tilde{p}^{\star\star\star}_p(\underline{\psi}, t) = (I + \Delta tS)\tilde{p}^{\star\star}_p(\underline{\psi}, t) \quad (33)$$

$$\tilde{p}_p(\underline{\psi}, t+\Delta t) = (I + \Delta tR)\tilde{p}^{\star\star\star}_p(\underline{\psi}, t) \quad (34)$$

The operator-splitting method provides the solution for the transport of $\tilde{p}$ by making use of a Monte Carlo technique. In the Monte Carlo simulation, the density-weighted PDF at each grid cell is represented by an ensemble of N_m stochastic elements where the ensemble-averaged PDF over N_m delta functions replaces the average based on a continuous PDF.[12]

$$\tilde{p}_{pm}(\psi) =< \tilde{p}_p(\psi) >= \frac{1}{N_m}\sum_{n=1}^{N_m}\delta(\psi-\phi^n) \qquad (35)$$

The discrete PDF $\tilde{p}_{pm}(\psi)$ is defined in terms of N_m sample values of ϕ^n, $n = 1, 2, 3...N_m$. The statistical error in this approximation is proportional to $N_m^{-1/2}$.

Using the operator-splitting method, the solution for the PDF transport equation is obtained sequentially according to the intermediate steps given by Eqs. (31)-(34).

9.2 Convection/Diffusion Step

The first step associated with convection/diffusion is given by:

$$\tilde{p}_p^*(\underline{\psi},t) = (I+\Delta tT)\tilde{p}_p(\underline{\psi},t) =$$
$$(1-\frac{c_p\Delta t}{\bar{\rho}\Delta V})\tilde{p}_p(\underline{\psi},t)+\sum_n\frac{c_n\Delta t}{\bar{\rho}\Delta V}\tilde{p}_n(\underline{\psi},t) \qquad (36)$$

This step is simulated by replacing a number of particles (= the nearest integer of $\frac{c_n\Delta tN_m}{\bar{\rho}\Delta V}$) at $\phi_p(t)$ by randomly selected particles at $\phi_n(t)$.

9.3 Numerical Issues Associated With Fixed Versus Variable Time Step

It is obvious from the above equation that a necessary criterion for stability requires satisfaction of $\frac{c_p\Delta t}{\bar{\rho}\Delta V} < 1$. When the computations are performed with a fixed time step, this criterion tends to be too restrictive for most applications. Depending on the flow configuration, the allowable maximum time increment Δt is likely to be limited by a region of the flow field where convective fluxes dominate (such as close to injection holes). But in the main stream, the flow is usually characterized by much lower velocities. Resolution considerations require a higher concentration of the grid in certain regions of the flowfield than in others. For example, more grid cells are clustered in regions where boundary layers are formed. In such regions the allowable maximum time increment might be limited in a direction dominated by the largest of the diffusive fluxes as determined by $\Gamma_\phi/\Delta x$. This problem gets magnified if the cells also happen to be highly skewed.

Such restrictions on the allowable maximum time step could lead to a frozen condition when the Monte Carlo simulation is performed with a limited number of stochastic particles per cell. For clarity, let us consider the following criterion:

$$N_m > \frac{\bar{\rho}\Delta V}{c_n\Delta t} \qquad (37)$$

which has to be satisfied at all grid nodes. It is estimated that about 10^3 stochastic particles per cell are needed in order to avoid the so-called frozen condition for performing a typical 3-D gas-turbine combustor calculation. The frozen condition is referred to a state in which no transfer of stochastic particles takes place between the neighboring cells when N_m falls below a minimum required. Scheurlen et al[27] were the first ones to recognize the limitations associated with the use of a fixed time step in the Monte Carlo PDF computations.

However, our experience has shown that this problem can be overcome by introducing the concept of local time-stepping which is a convergence improvement technique widely used in many of the steady-state CFD computations. In this approach, the solution is advanced at a variable time step for different grid nodes. In our present computations, it is determined based on

$$\Delta t = min(C_{tf}\Delta t_f, \frac{\rho\Delta V}{C_t(c_n+s_{mlc})}) \qquad (38)$$

where C_{tf} and C_t are calibrated constants and were assigned the values of 4 and 2.5, respectively, Δt_f is the local time step obtained from the flow (CORSAIR) module, and $s_{mlc} = \sum n_k m_k$. The time step is chosen such that it permits transfer of enough particles across the boundaries of the neighboring cells while ensuring that the time step used in the PDF computations does not deviate very much from the time step used in the flow solver.

9.4 Molecular Mixing Step

The second step associated with molecular mixing is given by:

$$\frac{d\phi_\alpha}{dt} = -C_\phi\omega(\phi_\alpha-\bar{\phi}_\alpha) \qquad (39)$$

The solution for this equation is updated by:

$$\phi_\alpha^{**} = \phi_\alpha^{*} + (\phi_\alpha^{*} - \bar{\phi}_\alpha^{*})e^{-C_\phi \omega \Delta t} \quad (40)$$

where C_ϕ was assigned a value of 1.

9.5 Spray Step

The third step associated with the spray contribution is given by:

$$\frac{d\phi_\alpha}{dt} = \frac{1}{\bar{\rho}\Delta V}\sum n_k m_k(\epsilon_\alpha - \phi_\alpha) \quad (41)$$

where $\phi_\alpha = y_\alpha, \alpha = 1, 2, ..., s = \sigma - 1$

$$\frac{d\phi_\alpha}{dt} = \frac{1}{\bar{\rho}\Delta V}\sum n_k m_k(-l_{k,eff} + h_{ks} - \phi_\alpha) \quad (42)$$

where $\phi_\sigma = h$. The solution for the above equations is upgraded by a simple explicit scheme:

$$\phi_\alpha^{***} = \epsilon_\alpha \frac{\Delta t \sum n_k m_k}{\bar{\rho}\Delta V} + \phi_\alpha^{**}(1 - \frac{\Delta t \sum n_k m_k}{\bar{\rho}\Delta V}) \quad (43)$$

where $\alpha \leq \sigma - 1$

$$\phi_\alpha^{***} = \frac{\Delta t \sum n_k m_k}{\bar{\rho}\Delta V}(-l_{k,eff} + h_{ks}) + \phi_\alpha^{**}(1 - \frac{\Delta t \sum n_k m_k}{\bar{\rho}\Delta V}) \quad (44)$$

where $\alpha = \sigma$. After a new value for enthalpy is updated, the temperature is determined iteratively from the solution of Eq. (10).

9.6 Reaction Step

Finally, the fourth step associated with chemical reactions is given by:

$$\frac{d\phi_\alpha}{dt} = -\nu_f \frac{W_f}{\rho} A(\frac{\rho\phi_f}{W_f})^a(\frac{\rho\phi_o}{W_o})^b e^{-(\frac{E_a}{T})} \quad (45)$$

where $\phi_\alpha = y_f$.

$$\frac{d\phi_\alpha}{dt} = -\nu_o \frac{W_o}{\rho} A(\frac{\rho\phi_f}{W_f})^a(\frac{\rho\phi_o}{W_o})^b e^{-(\frac{E_a}{T})} \quad (46)$$

where $\phi_\alpha = y_o$.

$$\frac{d\rho\phi_\alpha}{dt} = 0 \quad (47)$$

where $\phi_\alpha = h$.

The numerical solution for Eqs. (45)-(47) is integrated by an implicit Euler scheme.[28] The resulting non-linear algebraic equations are solved by the method of quasi-linearization.[29]

9.7 Details of Combustion Chemistry

In this section, we present an example of how combustion chemistry is handled for the case of n-heptane when it is modeled by a single-step global mechanism of Westbrook and Dryer.[30] The corresponding rate constants in Eqs. (45)-(46) are given by $A = 0.286\ 10^{+10}$, $a = 0.25$, $b = 1.25$, and $E_a = 0.151\ 10^{+05}$. This global combustion model is reported to provide adequate representation of temperature histories in flows not dominated by long ignition delay times. For example, the overall reaction representing the oxidation of the n-heptane fuel is given by:

$$C_7H_{16} + 11(O_2 + 3.76N_2) \rightarrow 7CO_2 + 8H_2O + 41.36N_2 \quad (48)$$

Because of the constant-Schmidt-number assumption made in the PDF formulation, based on atomic balance of the constituent species, the mass fractions of N_2, CO_2, and H_2O can be shown to be related to the mass fractions of O_2 and C_7H_{16} by the following expressions:

$$y_{H_2O} = K_2 - K_1K_2y_{O_2} - K_2y_{C_7H_{16}}$$

$$y_{CO_2} = K_3y_{H_2O} \quad (49)$$

$$y_{N_2} = 1 - K_2 - K_2K_3 - y_{O_2}(1 - K_1K_2 - K_1K_2K_3) - y_{C_7H_{16}}(1 - K_2 - K_2K_3)$$

where $K_1 = 4.29$, $K_2 = 0.08943$, and $K_3 = 2.138$.

Using Eq. (49) results in considerable savings in computational time as it reduces the number of variables in the PDF equation from five (four species and one energy) to three (two species and one energy).

9.8 Revolving Time-Weighted Averaging

It is noteworthy that although local time-stepping seems to overcome some of the problems associated with the PDF computations, the application of the Monte Carlo method requires the use of a large number of particles because the statistical error associated with the Monte Carlo Method is proportional to the inverse square root of N_m, thereby making the use of the Monte Carlo method computationally very time consuming. However, a revolving averaging procedure used in our previous work[31] seems to alleviate the need for using a large number of stochastic particles, N_m, in any one given time step. In this averaging scheme, the solution provided to the CFD solver is based on an average of all the particles present over the last N_{av} time steps instead of an average solely based on the number of particles present in any one single time step. This approach seemed to provide smooth Monte Carlo solutions to the CFD solver, thereby improving the convergence of the coupled CFD and Monte Carlo computations. The reason for improvement could be attributed to an effective increase in the number of stochastic particles used in the computations from N_m to $N_{av}N_m$. Here, it is assumed that the solution contained within different iterations of the averaging procedure is statistically independent of each other.

10 SPRAY SOLUTION ALGORITHM

In order to evaluate the initial conditions that are needed in the integration of the liquid-phase equations, we first need to know the gas-phase properties at each particle location. But in order to evaluate the gas-phase properties, it is first necessary to identify the computational cell where a particle is located. It is a trivial task to search for the computational cell of the particle location in rectangular coordinates. However, a search for the particle location becomes a complicated problem when the computational cell is no longer rectangular in the physical domain. An efficient particle-search algorithm is developed and implemented into the Lagrangian spray solver in order to facilitate particle movement in an unstructured grid of mixed elements. The search is initiated in the form of a local search from the computational cell of the previous time step as the starting point. The location of the computational cell is determined by evaluating the dot product of $\underline{x}_{pc} \cdot \underline{a}_n = |x_{pc}|\ |a_n|\ cos(\phi)$, where $\underline{x}_{pc}$ is the vector defined by the distance between the particle location and the center of the n-face of the computational cell, $\underline{a}_n$ is the outward area normal of the n-face as shown in Fig. 2, and ϕ is the angle between the two vectors.

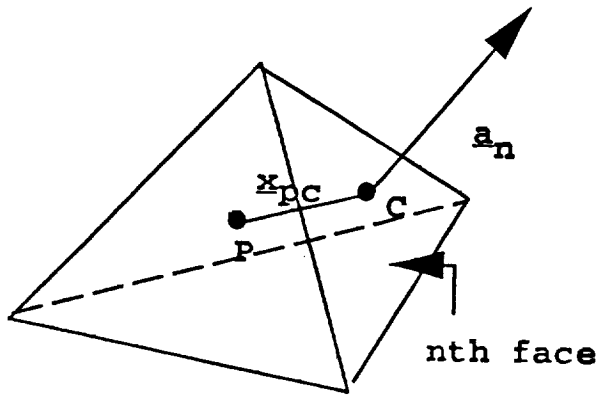

Figure 2 A vector illustration used in the particle search analysis.

A simple test for the particle location requires that the dot product be negative over each and every one of the n-faces of the computational cell. If the test fails, the particle search is carried over to the adjacent cells of those faces for which the dot product turns out to be positive. Some of those n-faces might represent the boundaries of the computational domain while the others represent the interfaces between two adjoining interior cells. The search is first carried over to the adjacent interior cells in the direction pointed out by the positive sign of the dot products. The boundary conditions are implemented only after making sure that all the possibilities lead to a search outside of the computational boundaries. This implementation ensures against any inadvertent application of the boundary conditions before locating the correct interior cell.

After the gas-phase properties at the particle location are known, the ordinary differential equations of particle position, size, and velocity are advanced by making use of a second-order accurate Runge-Kutta method. The partial differential equations governing the droplet internal temperature distribution are integrated by an Euler method. Finally, after the liquid-phase equations are solved, the liquid-phase source contributions to the gas-phase equations are evaluated.

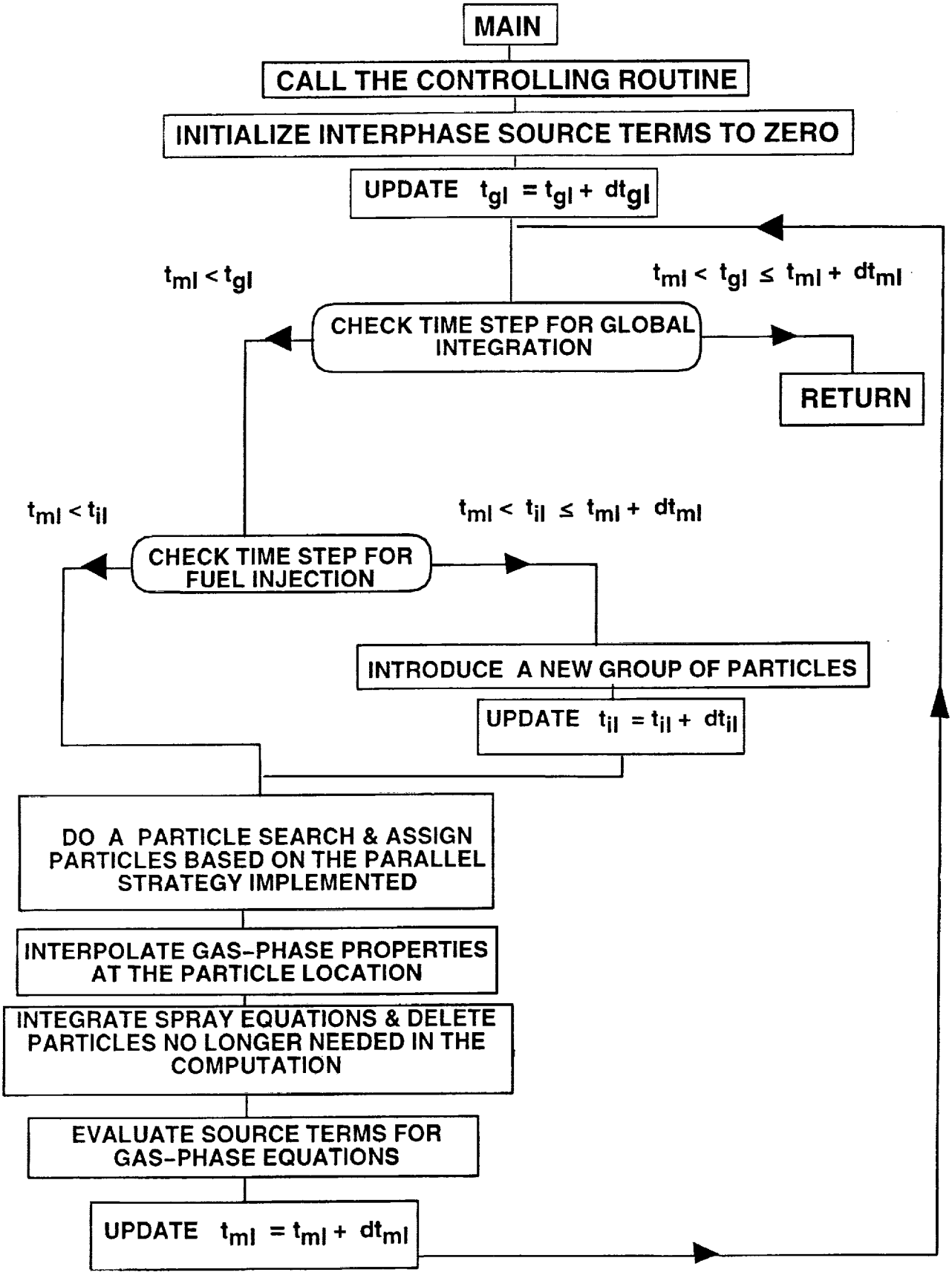

Figure 3 The flow structure of the spray code.

10.1 The Flow Structure of the Spray Code & Time-Averaging of the Interphase Source Terms of the Gas-Phase Equations

The spray solver makes use of three different time steps: Δt_{ml} is the allowable time step, Δt_{gl} is the global time step, and Δt_{il} is the fuel-injection time step. Δt_{ml} needs to be evaluated based on the smallest of the different time scales which are associated with various rate-controlling phenomena of a rapidly vaporizing droplet, such as those imposed by an average droplet lifetime, the local grid spacing and a relaxation time scale associated with droplet velocity among others. This restriction usually leads to a small time step which typically has values in the neighborhood of 0.01 milliseconds. However, our experience has shown that the convergence for the steady-state computations could be improved greatly by supplying the flow and PDF solvers with the interphase terms obtained from a time-averaging procedure, where the averaging is performed over an average lifetime of the droplets, Δt_{gl}. The variable, Δt_{gl}, has values in the neighborhood of 1 ms.

The averaging scheme could be explained better through the use of a flow chart shown in Fig. 3. The main spray solver is invoked by a call to the controlling routine which executes the following steps:

1. It first initializes the source terms to zero.
2. Checks to see if new particles need to be introduced.
3. Advances liquid-phase equations over a prespecified time step, Δt_{ml}, with calls to the following routines:
   - Does a particle search and assigns particles based on the parallel strategy implemented.
   - Interpolates gas-phase properties at the particle location.
   - Advances liquid-phase equations and, also, deletes any particles that are no longer needed in the computations.
4. Evaluates the liquid-phase source-term contributions, S_{ml}, for use in the gas-phase equations.
5. Continues with steps (2) and (3) until the computations are completed over a global time step of Δt_{gl}.
6. Returns control to other solvers, e.g., flow or PDF, and supplies them with source terms, S_{gl}, averaged over Δt_{gl}.

The time-averaged contribution of these source terms, S_{gl}, is given by:

$$S_{gl} = \sum_{m=1}^{M} \frac{\Delta t_{ml}}{\Delta t_{gl}} S_{ml} \tag{50}$$

where

$$\sum_{m=1}^{M} \Delta t_{ml} = \Delta t_{gl} \tag{51}$$

11 COUPLING BETWEEN THE THREE SOLVERS

For the PDF solver, the mean gas-phase velocity, turbulence diffusivity and frequency are provided as inputs from the CFD solver and the modeled spray source terms from the liquid-phase solver. And, in turn, the Monte-Carlo solver supplies the temperature and species fields to the other two solvers. The CFD code also receives the liquid-phase source terms as inputs from the spray solver. For the spray solver, the needed gas-phase velocity and scalar fields are supplied by the other two solvers. The liquid-phase, PDF, and CFD solvers are advanced sequentially in an iterative manner until a converged solution is obtained. It should also be noted that both the PDF and spray solvers are called once at every specified number of CFD iterations. All three PDF, CFD, and spray codes were coupled and parallelized in such a way in order to achieve maximum efficiency.

12 RESULTS AND DISCUSSION

The calculation procedure was applied to predict the flow properties of an unconfined spray flame for which some experimental data was reported by McDonnel and Samuelson.[20] We also discuss the results from a 3D test case which was designed to demonstrate the viability of the present solution procedure for use in 3D computations.

12.1 Unconfined Spray Flame

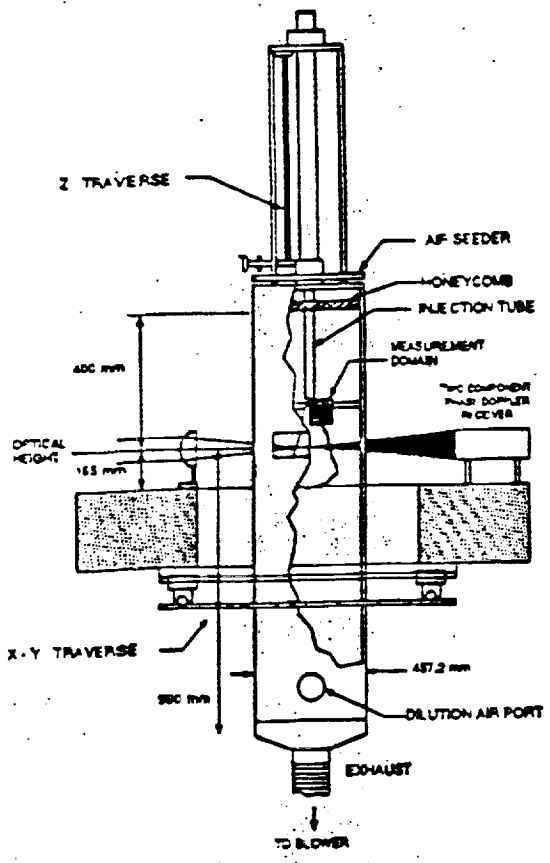

Fig. 4 Schematic of the spray burner facility (McDonell & Samuelson).

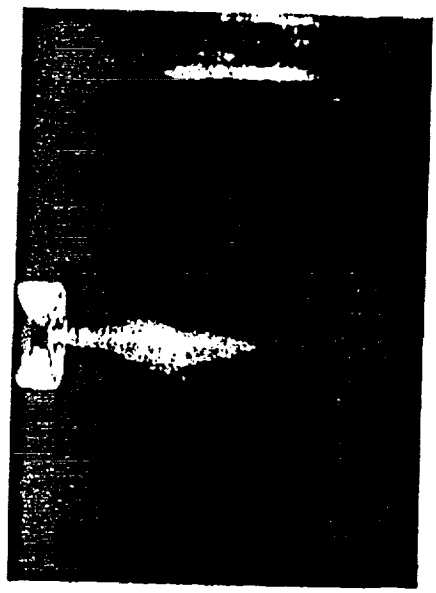

Fig. 5 Photograph of a reacting non-swirling spray (McDonell & Samuelson).

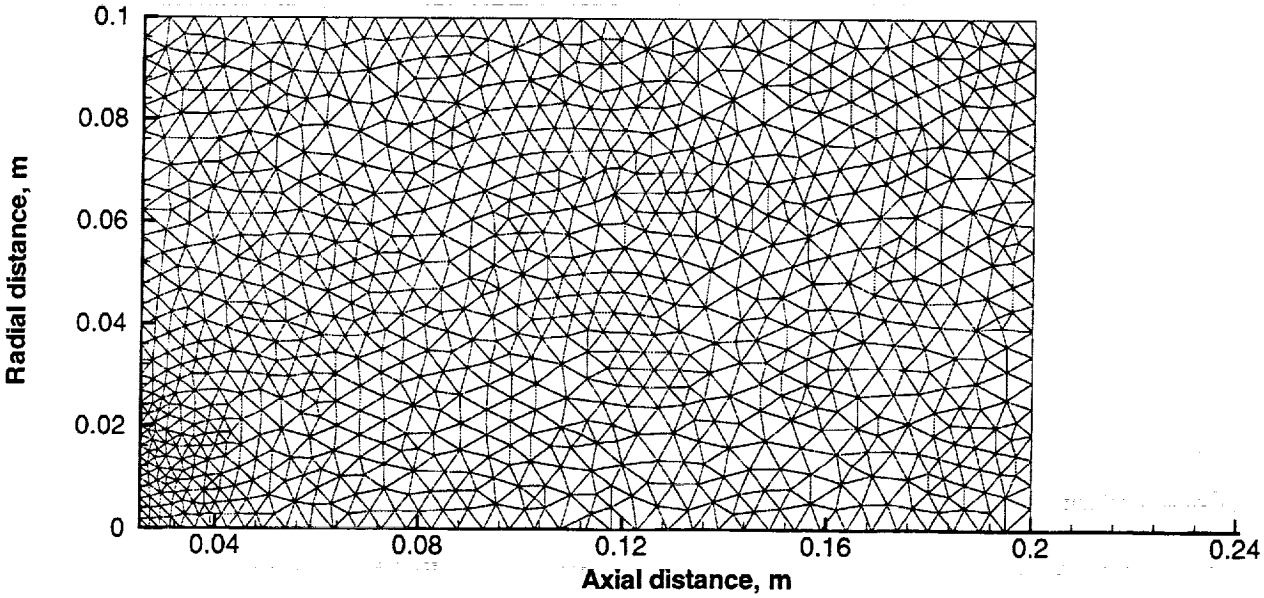

Fig. 6 2D computational grid of McDonell & Samuelson (1850 elements).

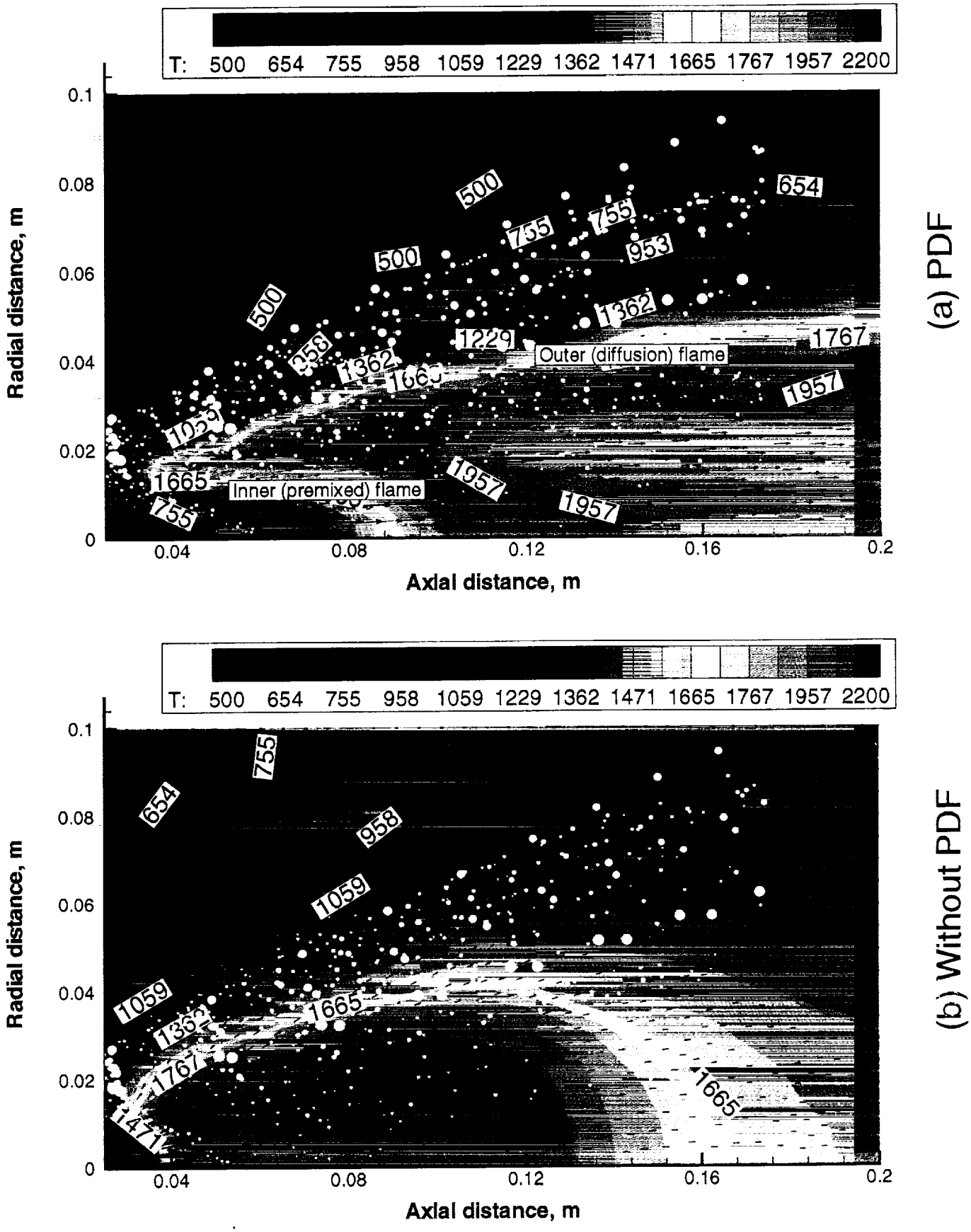

Fig. 7 Global structure of a spray flame.

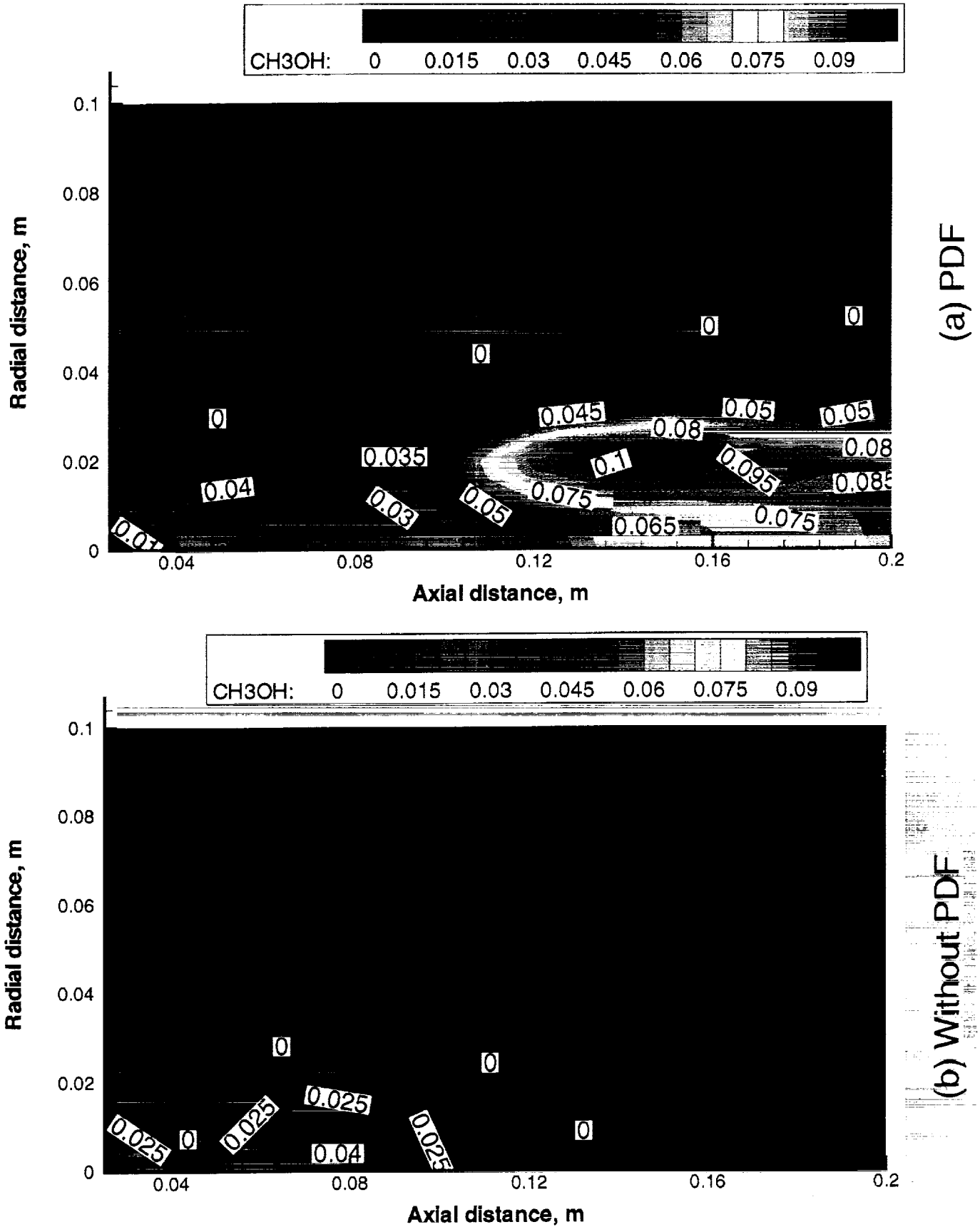

Fig. 8 Fuel mass fractions contours.

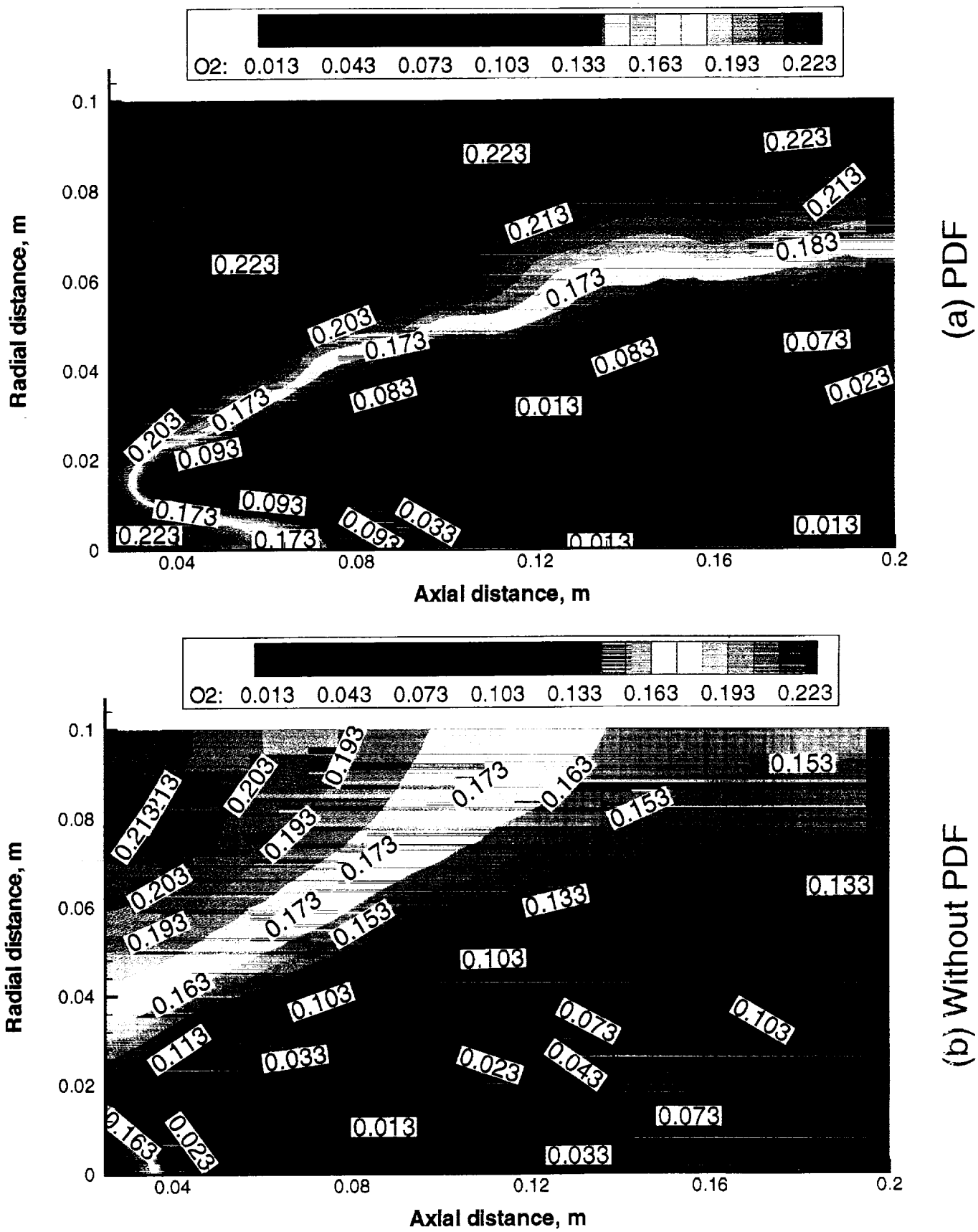

Fig. 9 Oxygen mass fraction contours.

A detailed experimental data set for the case of an unconfined methanol spray was reported by McDonnel and Samuelson.[20] The schematic of the experimental facility used at UCI (University of California, Irvine) is shown in Fig. 4. It made use of a Parker and Hannifin RSA (Research Simplex Atomizer) whose simplex tip has a flow number of 1.36 and a nominal spray angle of 85 degrees. The reported methanol and air mass flow rates were 1.26 and 1.32 g/s, respectively. The spray was injected downwards from the center of a 495 x 495 mm square duct and air was pulled through the top of the duct by a blower at a bulk velocity of 0.8 m/s in order to provide adequate entrainment needs. Both the droplet and gas-phase velocities as well as the droplet sizes were measured by making use of a two-component PDI (Phase Doppler Interferometry), and the gas-phase temperatures were measured by using a traversing hot-wire thermocouple. Using the setup shown in Fig. 4, several measurements involving the gas-phase velocity, droplet size and velocity, droplet number flux, and mean gas-phase temperatures were reported at different axial locations starting from 2.5 cm.

A photograph of the burning spray is shown in Fig. 5. For the case considered, it produces a narrow illuminating flame at the center.

For the axisymmetric configuration, both the PDF and non-PDF computations were performed on a 2D grid of 1850 triangular elements as shown in Fig.6. Since in complex 3D geometries, it is not always possible to identify and delineate critical regions of a flow-field, a relatively coarse mesh was chosen to see how well the flow-field could be computed without resorting to a fine grid. The turbulent Schmidt and Prandtl numbers were taken to have a value of 0.70. The PDF solution was obtained by making use of 100 particles per cell. The temperature and species fields supplied to the CFD and liquid-phase solvers were obtained from averaging the PDF solutions over a period of the last 100 time-steps. The calculations were advanced until a steady state solution was reached by making use of the following time steps: Δt_g was determined based on a local time-step with a CFL number of 1, $\Delta t_{injection}$ = 1.0 ms, and Δt_k = 0.01 ms. At the end of every liquid-phase injection time step, a new droplets group was introduced.

12.1.1 Global Features of the Spray Flame

The global features of the spray flame are shown in Figs. 7a and 7b by presenting a composite view of the droplet locations and the mean gas-phase temperatures and velocity vectors. The filled white circles show the location of the droplets. The droplet sizes range from few microns to 140 microns. The shaded contour lines show the temperature distribution, and the arrows denote the velocity vectors. Fig. 7a shows the results from the PDF method and Fig. 7b from the non-PDF (conventional CFD) method.

First, let us first look at the droplet distribution. As expected, because of the prevailing high temperatures, the droplets in the central region of the spray tend to vaporize faster than those present in the outer regions of the spray. For that reason, the average size of the droplets in the central region is much lower than those present elsewhere. However, most of the droplet mass is contained within the droplets of the high temperature region. The largest droplets found outside of the high-temperation region are sometimes called in the literature as rogue droplets.[20]

Next, let us look at the results from the PDF computations. Combustion seems to be initiated by a flame front stabilized in the lower velocity region of the outer shear layer. Starting from there, the high temperature region spreads in a long v-neck shape as a result of two distinct flames being formed. The inner flame has the characteristics of a turbulent premixed flame and the outer flame shows the characteristics of a turbulent diffusion flame. The distinction between the two flames becomes more obvious when we will look at the fuel and oxygen mass-fraction contour plots shown in Figs. 8 and 9. Methanol is known to vaporize rapidly, its vapor has the same density as air, and its liquid saturation temperature is approximately around 263 K which can easily be achieved prior to atomization.[20] Early vaporization and mixing of fuel vapor with air leads to the formation of an inner premixed flame. Further vaporization leads to a large accumulation of fuel vapor inside of the central high-temperature region (Fig. 8a). This region is also devoid of oxygen (Fig. 9a). Here, combustion takes place with the formation of a diffusion flame where the fuel from the inner central region mixes and burns with the surrounding air from the outer region. However, it is noteworthy that in sprays this kind of characterization of attributing the flames to be either premixed or diffusion could only be made in a general sense. Because of vaporizing droplets present within an active flame zone, it makes any kind of strict characterization meaningless.

On the other hand, the non-PDF computations in Fig. 7b show for the combustion to occur in a pre-

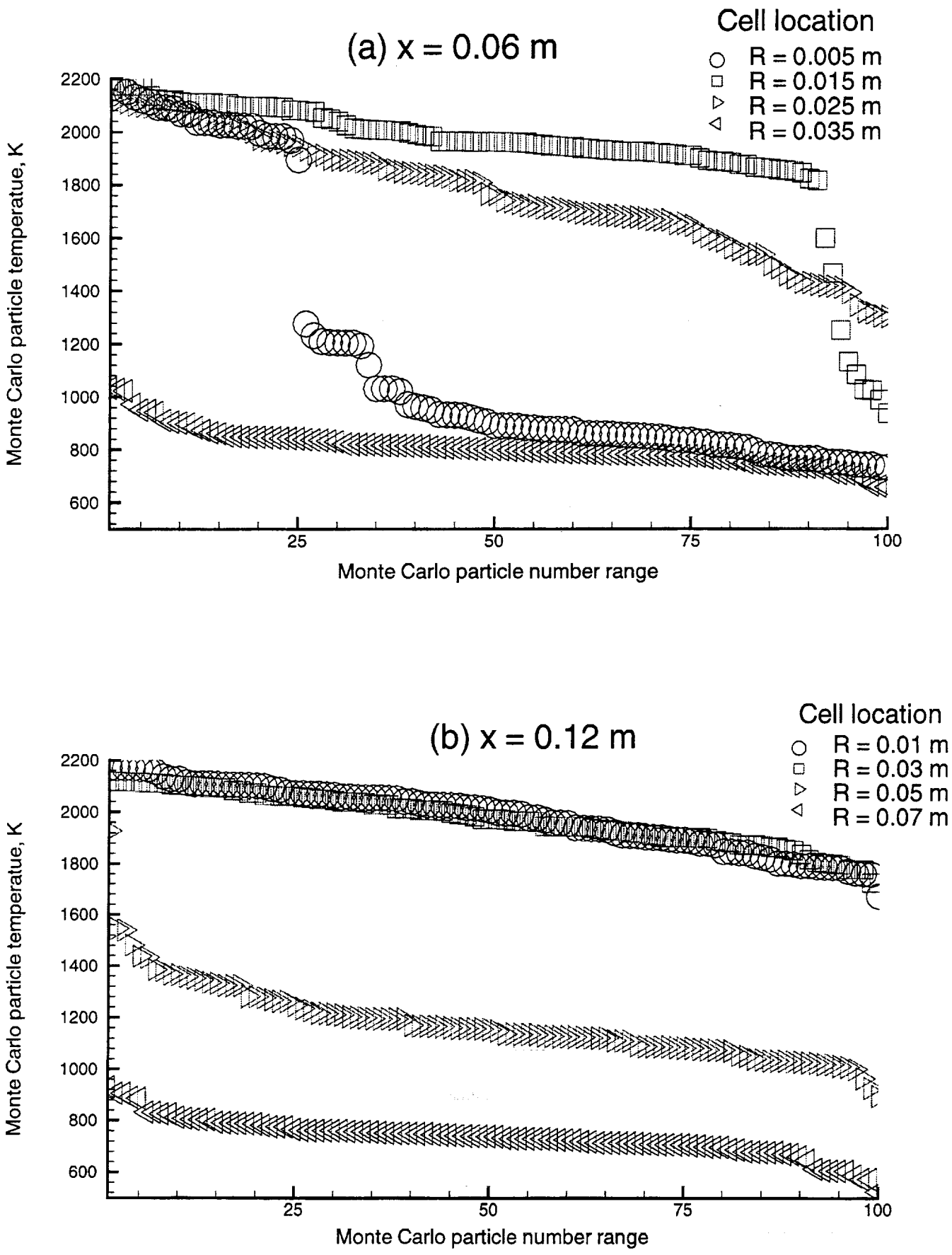

Fig. 10 Monte Carlo particle temperature distribution at four different computational cells.

dominantly vaporization-controlled reaction regime. As a result, the high temperature region is spread over a wider region. It lacks a well-defined flame structure that was observed with the PDF computations.

Near the centerline, the PDF results show for the jet to retain its axial momentum better than the non-PDF solution. The PDF results also show less radial spreading of the jet further downstream. As we sill see later, the PDF results are more in compliance with the experimental data than those predicted by the non-PDF calculations.

12.1.2 Gas-Phase Mass Fraction Contours

Figs. 8 an 9 show the mass fraction contours of methanol and oxygen, respectively. First, looking at the methanol mass fractions reinforces the remarks that were made earlier on the PDF results. Early vaporization leads to an accumulation of fuel vapor in the inner core region of the jet which supports a premixed inner flame (Fig. 7a). But, further downstream, there is a large accumulation of fuel vapor in the the region where high-temperature products are present. This fuel-rich region is also devoid of oxygen (Fig. 9a). Mixing of this fuel vapor with the surrounding outer air supports a diffusion flame. However, this outer flame also feeds on the fuel vapor from the vaporizing droplets present in its active combustion region. The oxygen mass fractions (Fig. 9a) also show clearly a well-defined flame structure.

However, the non-PDF computations show a slight accumulation of fuel vapor in only a small region of the entine domain which implies instantaneous burning of the vaporized fuel. Unlike the PDF predictions, the oxygen mass fractions lack a well-defined flame structure as combustion seems to occur over a much wider region in a vaporization-controlled regime.

12.1.3 Gas-Phase Monte Carlo Particle Temperature Distribution

In order to examine further what is causing the major differences found in the PDF and non-PDF results, let us take a look at the scatter plots of the Monte Carlo particle temperature distribution shown in Figs. 10a-b. Fig. 10a contains the particle distribution at four different radial nodes of an axial location at 0.06 m, and Fig. 10b provides similar information at an axial location of 0.12 m. The particle temperatures shown here have been pre-sorted to fall in a descending order.

Referring to Fig. 7a, it is obvious that the four nodes at the first axial location are chosen to examine the differences in the Monte Carlo particle distribution associated with the inner and outer flames. The second axial location is chosen to examine the differences further downstream.

The first node is from the central region region of the jet, and it falls in the the outer (reactants) region of the inner (premixed) flame. The second and third nodes are located close to the active flame zones of the inner and outer flames, respectively. And the fourth one falls in the outer (surrounding air) region of the outer (diffusion) flame.

In the first node, few of the particles are at flame temperature and most of the rest are at a lower temperature of the surrounding reactants. In the next cell, most of the particles are at a flame temperature and it is followed by an abrupt drop near the end. The abrupt changes in the temperature distribution at the first two locations are indicative of the intermittency effects associated with a turbulent premixed flame. It is obvious that the inner flame is characterized by large fluctuations in temperature. If the corresponding PDFs were constructed, the PDFs would show two distinct peaks of varying amplitudes depending upon the proximity to the flame front. One of the peaks is centered around the flame temperature and the other at the temperature of the surrounding reactants.

The particles distribution in the next two cells are associated with the outer diffusion flame. Unlike the inner flame, the particle distribution for the outer flame is mainly characterized by a single peak with the temperatures ranging between 2100 to 1400 K at the third cell and 1000 to 900 K at the fourth cell. However, the PDF at the third location (near the flame) would show a distribution over a wider temperature range with a relatively large variance compared to one associated with the fourth location.

Figure 10b shows a small variance at the first two cells with a mean closer to the flame temperature. The small variance in the temperature is due to the changes in the composition of the product gases which are caused by the addition of fuel vapor from the vaporizing droplets. The particle distribution in the next two nodes is essentially what one expects to see in the outer surrounding regions of a typical diffusion flame. As expected, the mean temperature shows the inverse functional relationship with the increasing normal distance away from the flame front.

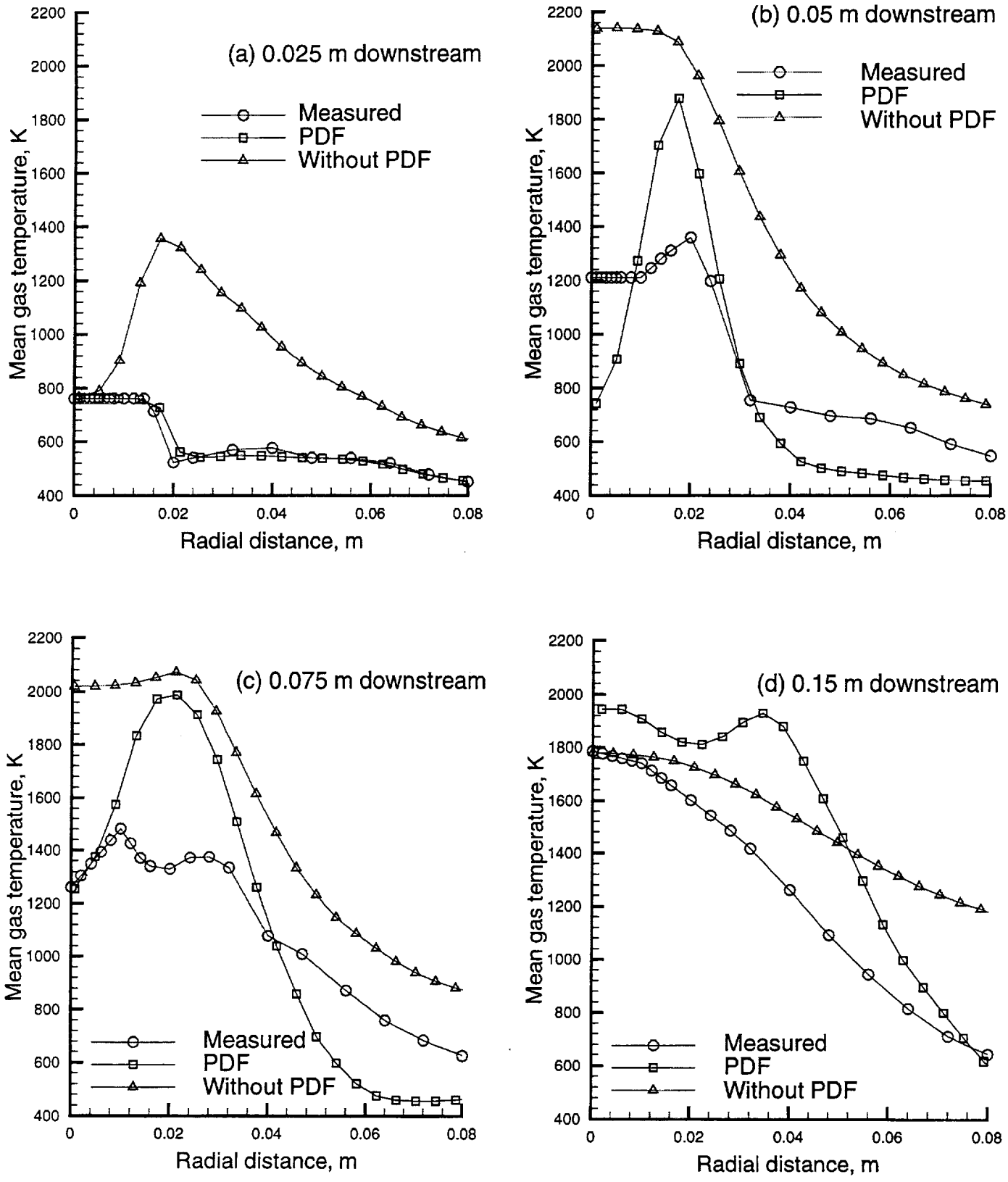

Fig. 11 Gas-phase mean temperature comparisons.

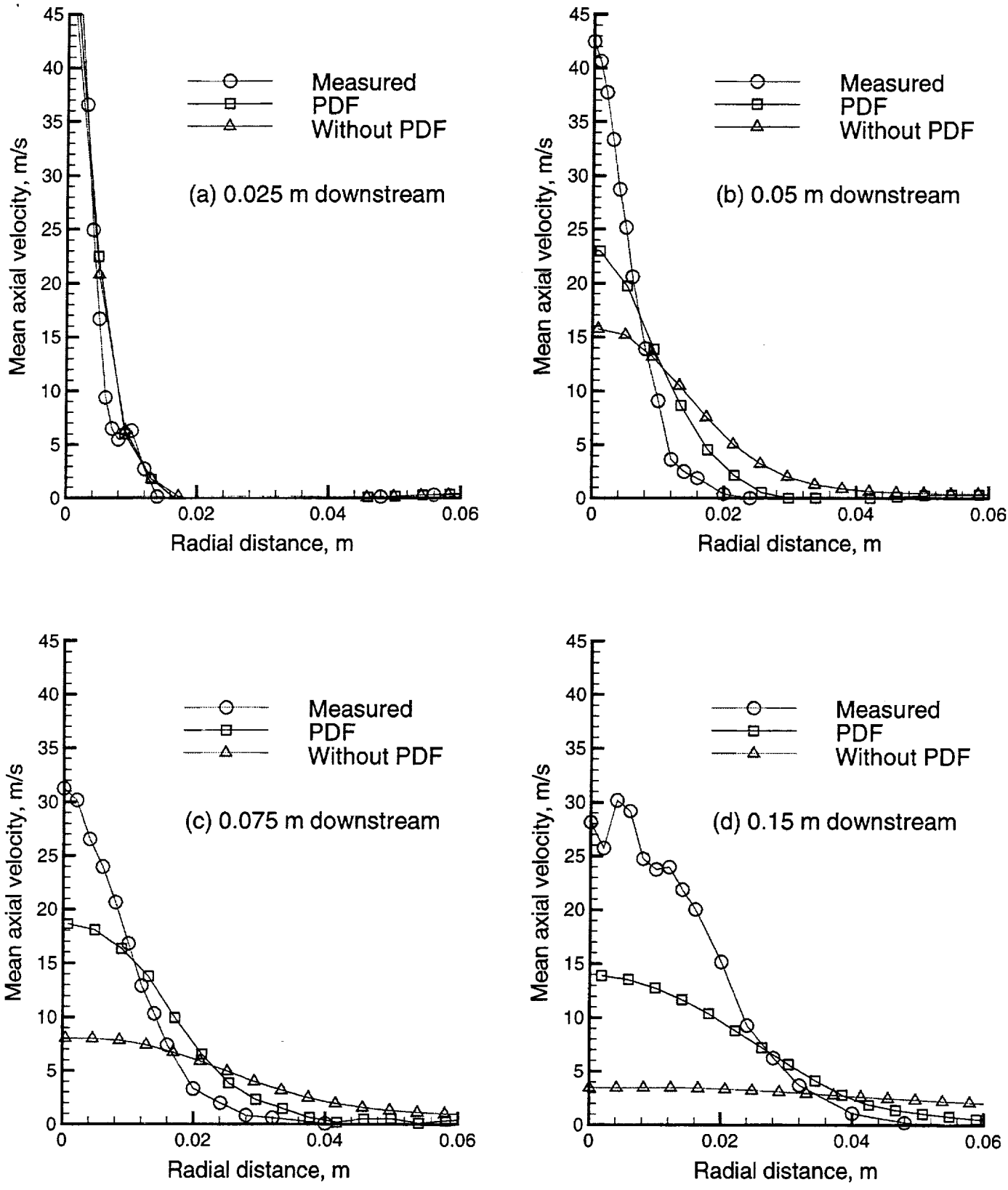

Fig. 12 Gas-phase mean axial velocity comparisons.

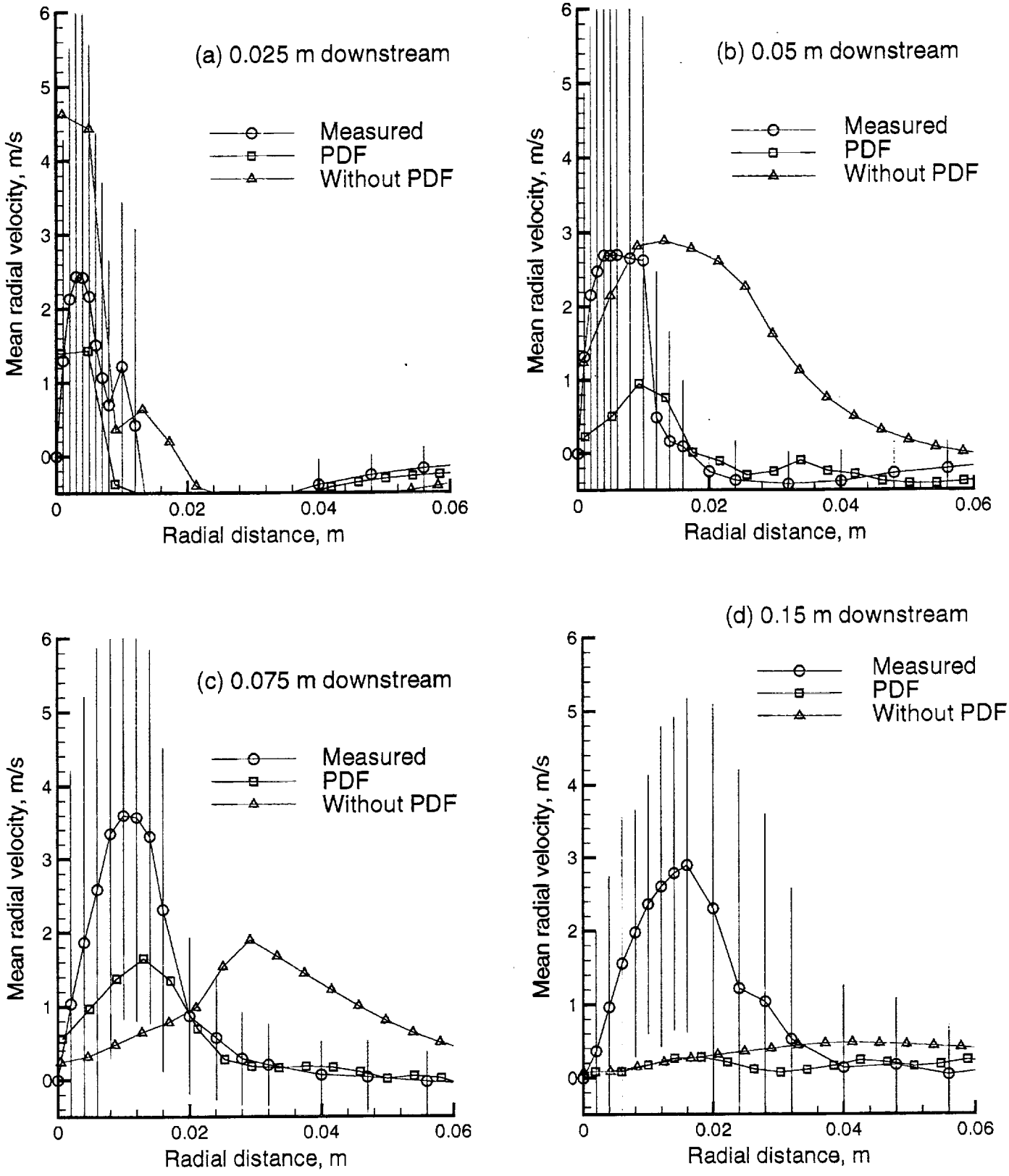

Fig. 13 Gas-phase mean radial velocity comparisons (experimental rms is shown as an error bar).

12.1.4 Mean Gas-Phase Temperature Comparisons

Figs. 11a-d show the comparisons for the radial profiles of mean gas temperature at four different axial locations. Both the PDF and non-PDF computations seem to predict higher peak temperatures than those measured. Some of the differences found could be attributed for the following reasons:

(1) The wetting of the thermo-couples might have contributed to some of the uncertaininty observed in the the reported temperatures. For this reason, the comparisons in this section are mainly meant to provide a qualitative description.

(2) The uncertainty contained in the experimental data is not clear because no error bands were provided for the data reported.

(3) Even though ethanol flame temperature is about 2100 K under normal conditions, the maximum attainable temperature is also a function of the initial temperature of the gas mixture. The bulk inflow temperature of about 500 K is higher than the normal ambient temperature which leads to a correspondingly higher flame temperature.

(4) The use of a single-step global mechanism is known to overpredict the flame temperatures by about 100 to 200 K.

(5) Some of the temperature drop could be attributed to the higher emissivity and radiation cooling rate of the spray combustion flame.

At the inflow in Fig. 11a, if one is wondering why should there exist any differences at all between the measured and computed (both PDF and non-PDF) temperatures, it is because the predictions represent the temperatures extrapolated from those known at the cell centers instead of those specified on the boundary faces of the cells where the inflow conditions were applied. In Fig. 11a, the PDF results show very little change from the specified inflow temperatures, and the results are very close to the specified the experimental data. However, the non-PDF computations show an abrupt jump from the specified inflow temperatures.

At the next location in Fig. 11b, the non-PDF shows the formation of a hot central region with the centerline peak reaching a flame temperature of about 2200 K. Unlike the non-PDF, both the measured and the PDF show for the temperature to peak in the outer region of the spray, and the peak temperature location is correctly predicted by the PDF computations. However, the PDF underpredicts the centerline temperature while overpredicting the peak temperature. If you recall from our earlier discussion on the temperature fluctuations in this region, it is quite likely that the measuring devices (thermocouples) may have difficulty in capturing the correct mean temperatures in this region. Farther away from the outer region of the spray, there is no physical explanation as to why the measured temperatures are higher than those predicted by the PDF other than any differences stemming from the neglect of radiative heat transfer.

At the third location, near the centerline, the PDF results are in compliance with the measured data. At the last two locations, the PDF again correctly predicts the location of the peak temperatures. But, in both locations, the PDF clearly overpredicts the peak temperatures while underpredicting the temperatures in the outer regions of the spray. On the other hand, the non-PDF results show a further broadening of the central high-temperature region and a greater radial temperature spreading into the outer region.

12.1.5 Gas-Phase Velocity Comparisons

Figs. 12a-d show the comparisons for the mean gas-phase axial velocities at four different axial locations. As expected near the inflow, both the predictions and measurements show similar behavior as shown in Fig. 12a. But at the next three downstream locations of Figs. 12b-d, both the PDF and non-PDF predictions underpredict the velocities near the centerline. The PDF predictions are more closer to what was observed experimentally, and the comparisons become progressively worse further downstream with the non-PDF computations.

The radial velocity comparisons are shown Figs. 13a-d. It is noteworthy that the experimental data seem to show a great deal of noise when it comes to measuring the radial velocities. For that reason, the rms component of the radial velocity is superimposed as a vertical error bar. The error bars clearly show that the fluctuations are indeed very large and in some instances even exceed the corresponding mean. Similar noise was reported in the data used in our previous comparisons of a swirl-stabilized spray case.[9,32] The PDF correctly predicts the locations of the peaks at all four locations but seem to underpredict the magnitudes by a considerable measure. However, the non-PDF computations tend to overpredict the radial distances of the peak, and the comparisons become progressively worse further downstream.

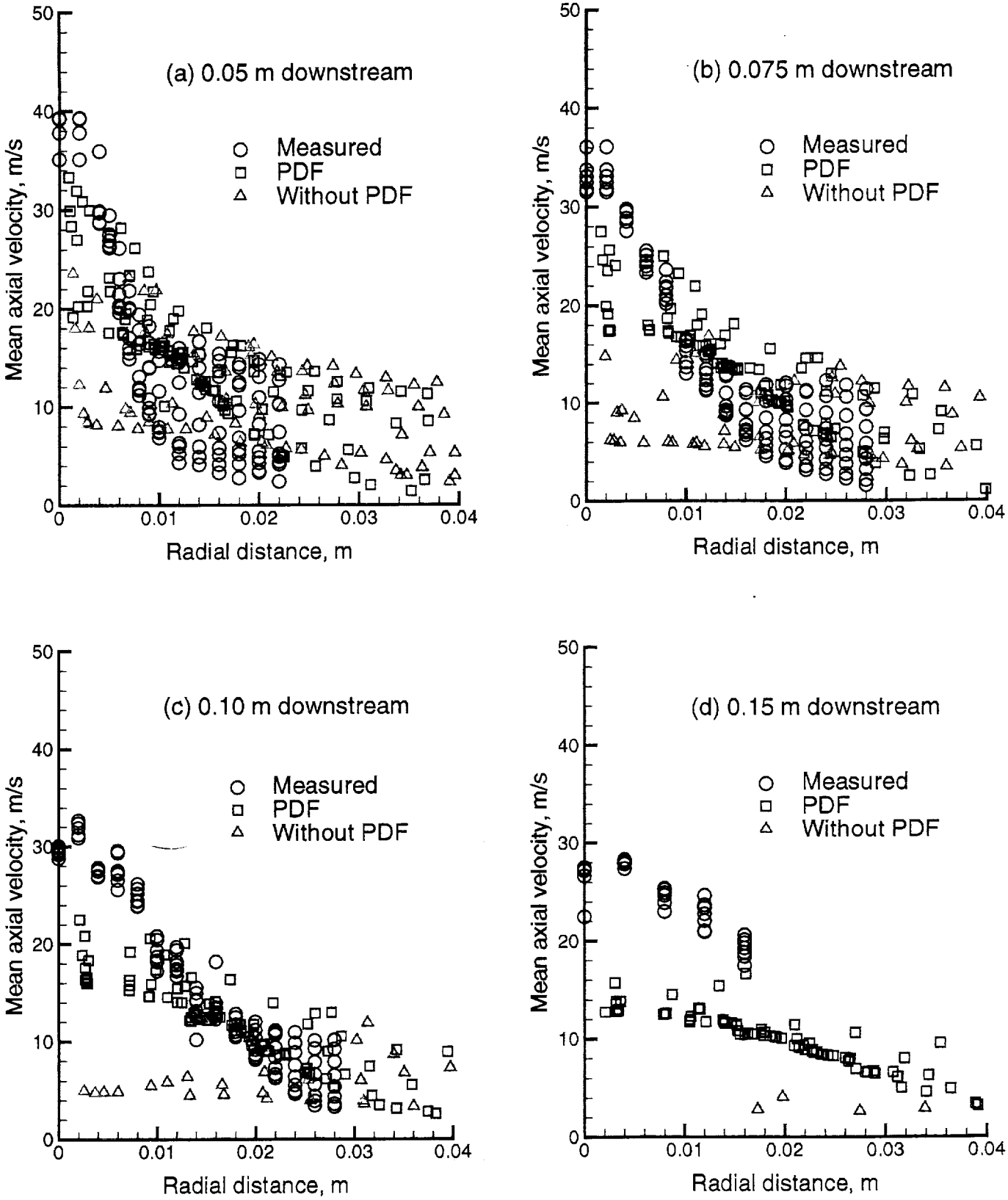

Fig. 14 Drop mean axial velocity comparisons.

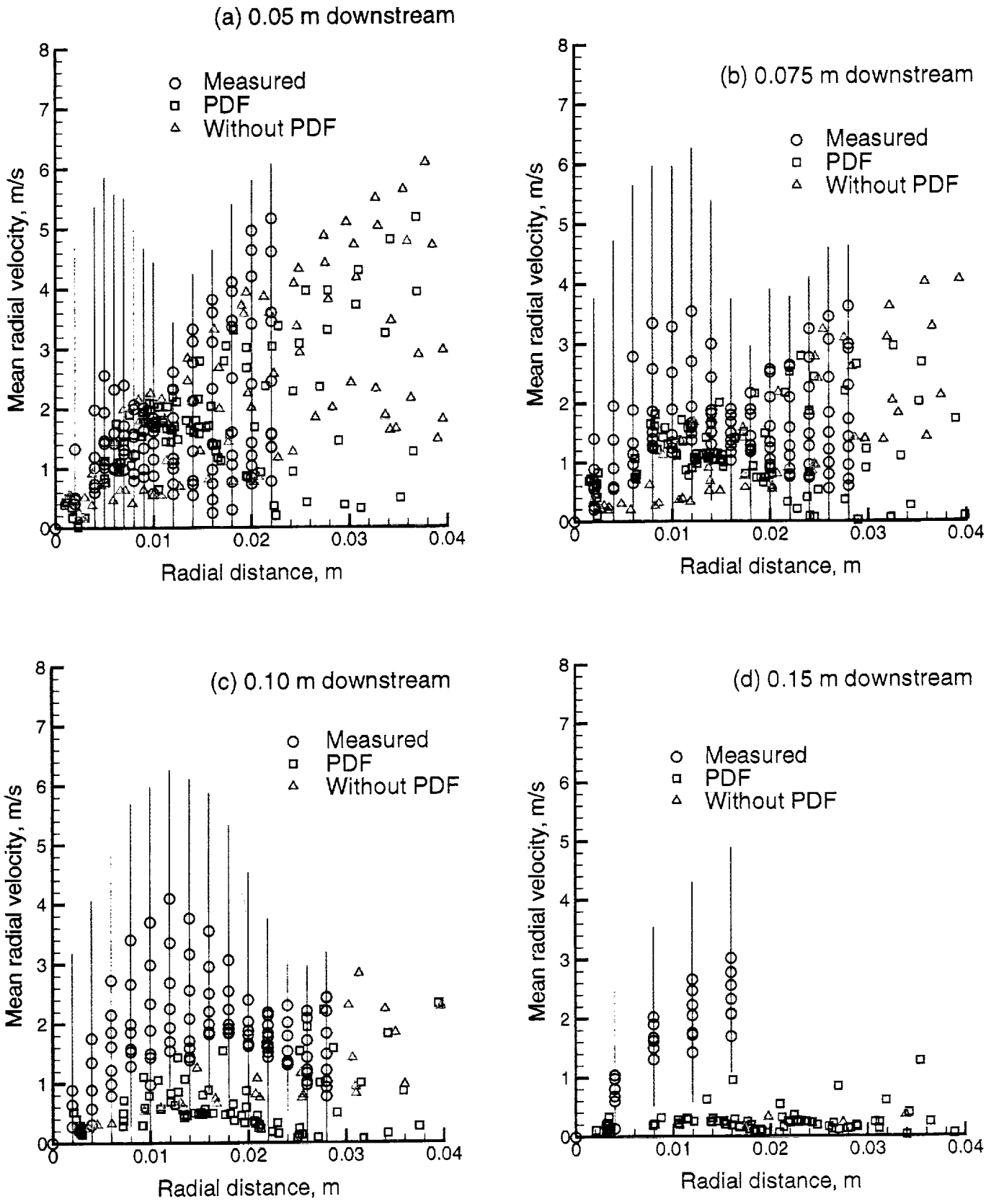

Fig. 15 Drop mean radial velocity comparions (experimental rms is shown as an error bar).

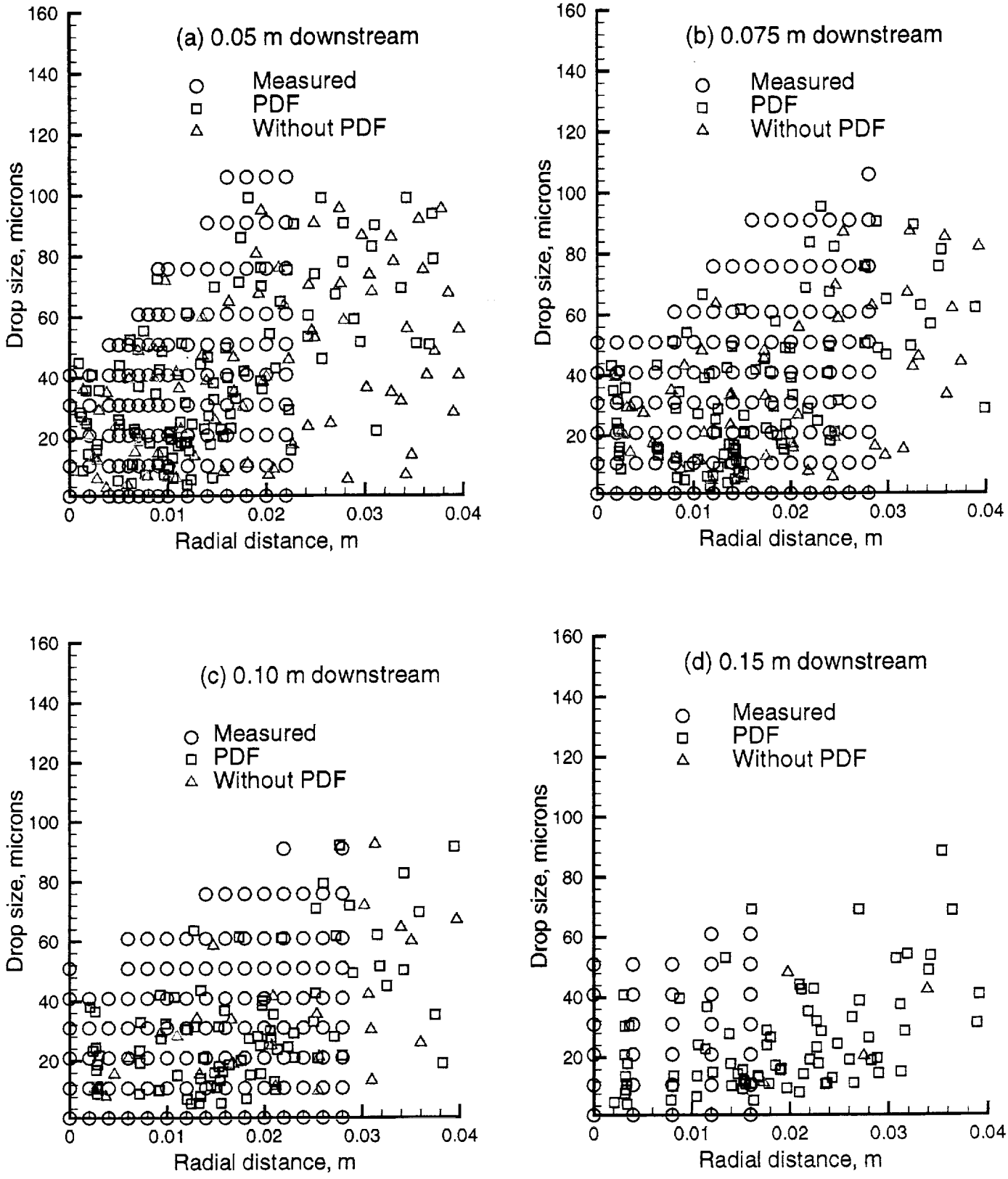

Fig. 16 Scatter plot of drop size comparisons.

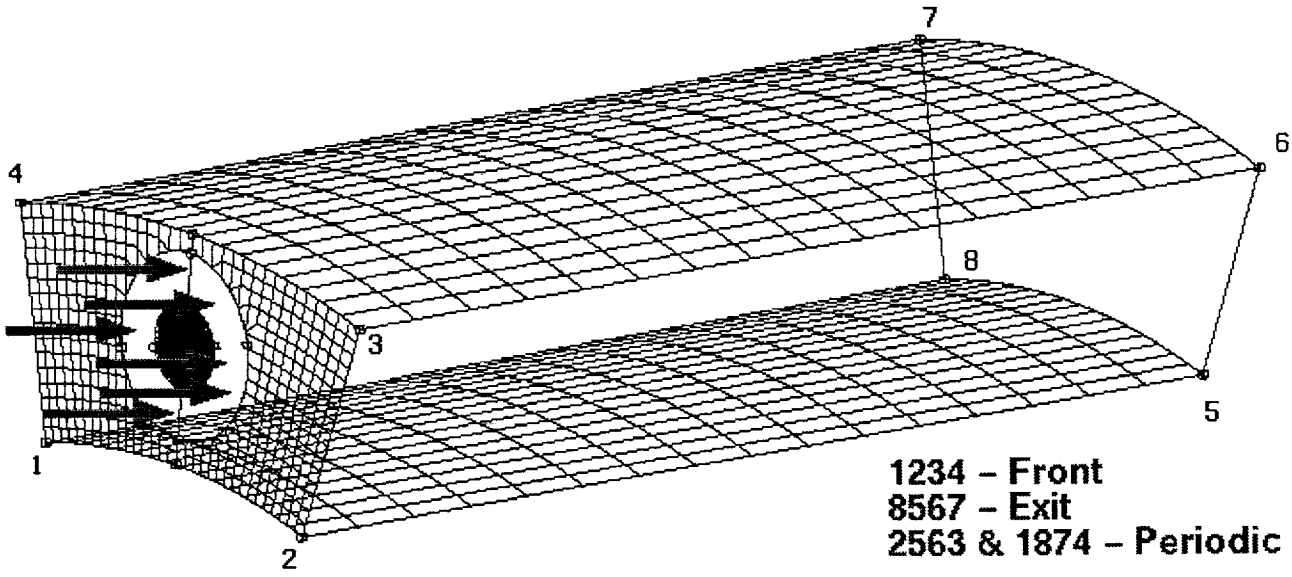

Fig. 17 Schematic of a 3D test case.

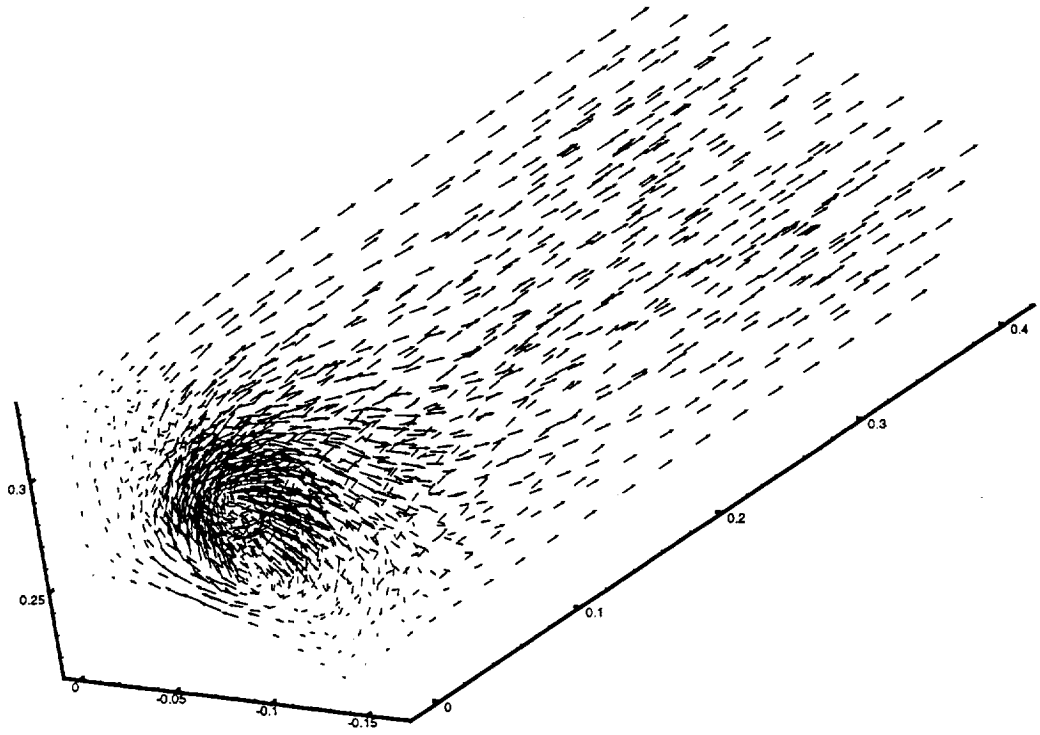

Fig. 18 Velocity vector plot of a 3D test case.

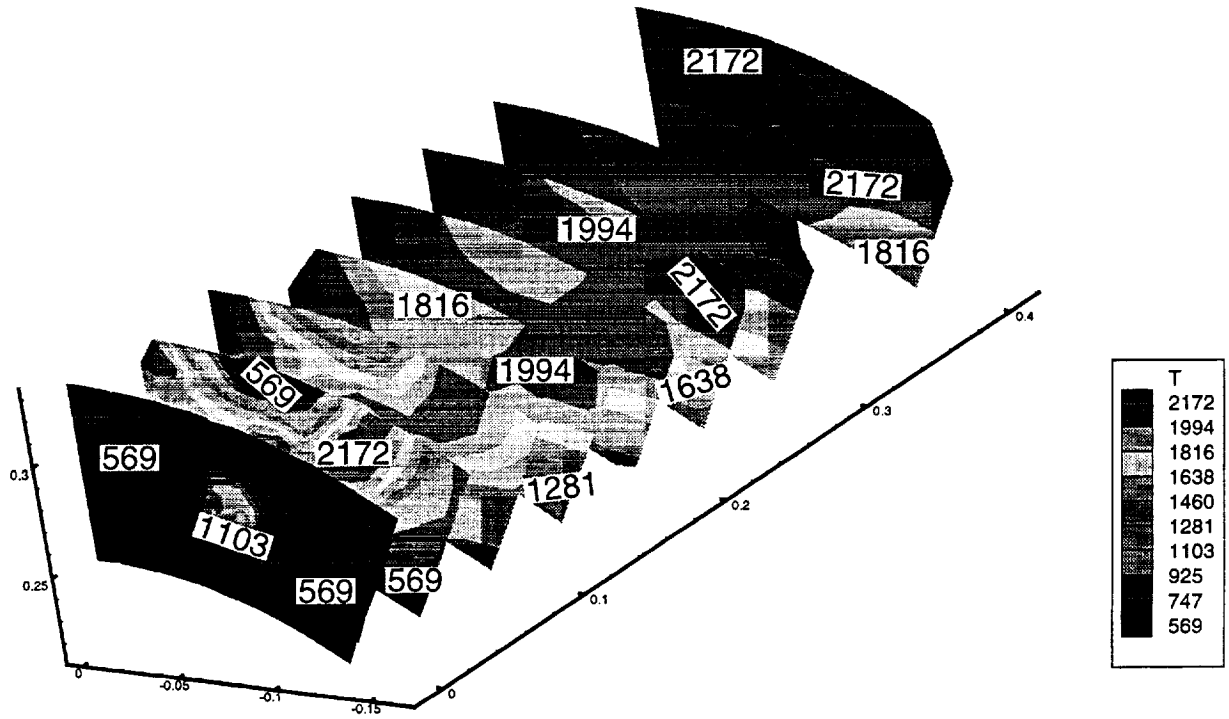

Fig. 19 Temperature distribution of a 3D test case.

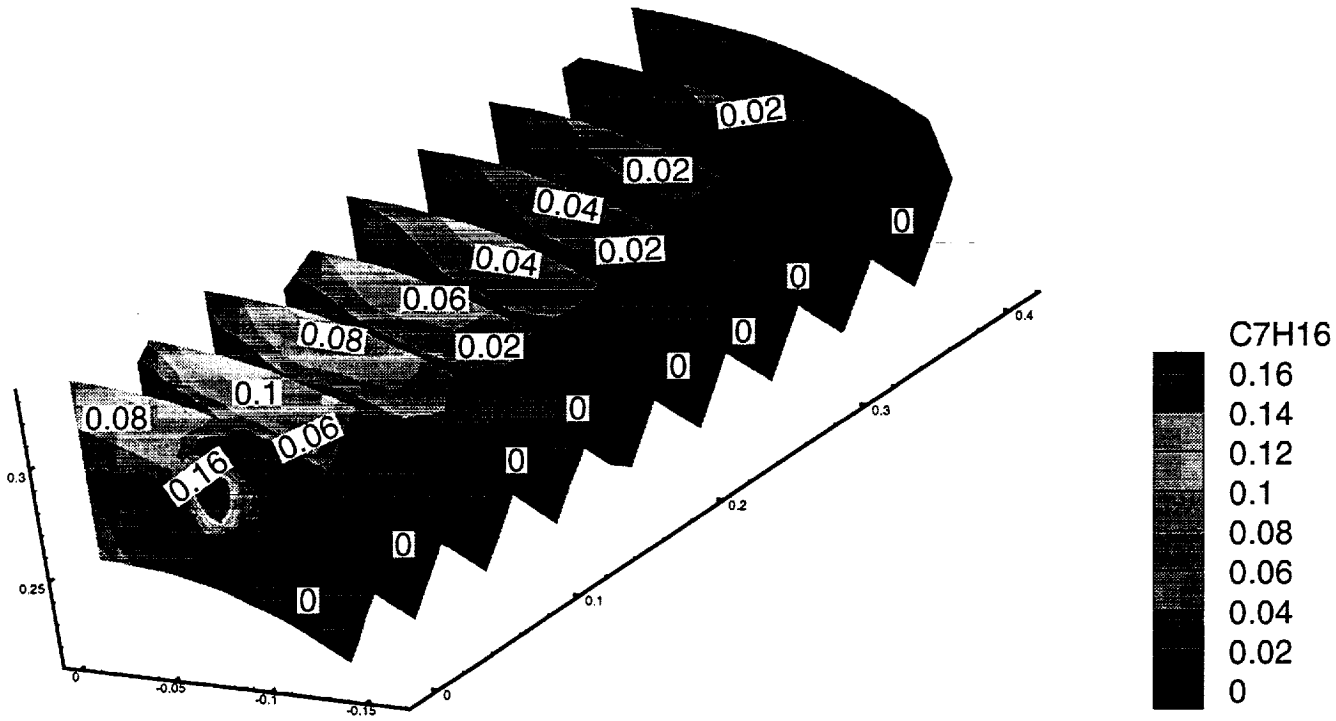

Fig. 20 Fuel mass fraction contours of a 3D test case.

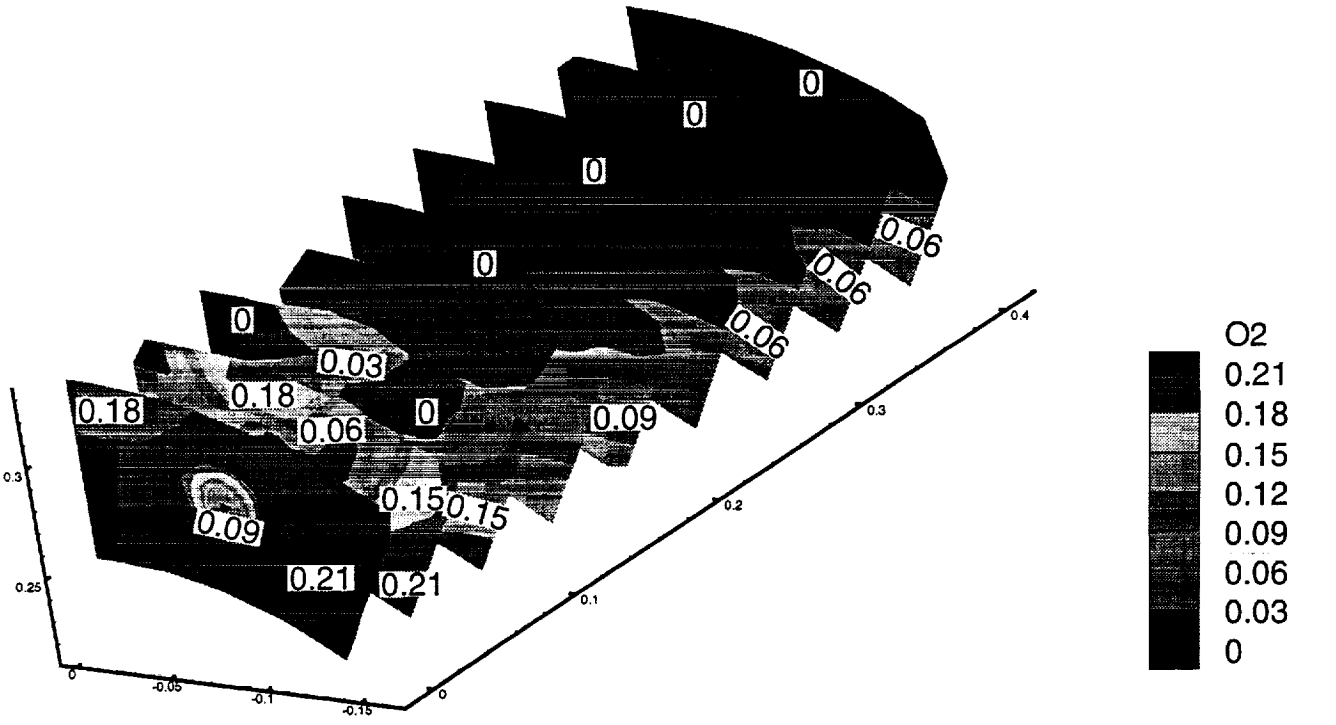

Fig. 21 Oxygen mass fraction contours of a 3D test case.

12.1.6 Droplet Velocity & Size Comparisons

The scatter plots of the mean droplet axial velocity are presented in Figs. 14a-d at four different axial locations. These plots include all of the reported measured velocities as well as the Lagrangian particle velocities. The experimental reported data is only limited to measurements in the radial direction of 0.02 m from the centerline distance.

The PDF seems to provide a better agreement than the non-PDF, and the non-PDF comparisons become progressively worse further downstream. These comparisons are consistent with the mean gas-phase velocity comparisons discussed earlier. The differences observed near the centerline with the PDF predictions could partially be attributed to the corresponding behavior observed earlier in the gas-phase velocities. As we have discussed earlier, because of the high temperatures that existed in the central region of the jet, the droplet sizes on the average in that region tend to be smaller because they vaporize faster. This would in turn cause the droplets to relax toward the surrounding gas-phase velocities much faster because of the drag forces acting on the smaller droplets.

Figs. 15a-d show the scatter plots of mean droplet radial velocity. As in the gas-phase, the experimental data show a great deal of noise when it comes to measuring the radial velocities. The error bars based on the rms component clearly show that the fluctuations are very large and in some instances even exceed their corresponding mean. Both the PDF and non-PDF comparisons underpredict the experimental data. The PDF computations are able to capture the qualitative trends correctly but the non-PDF comparisons become progressively worse further downstream.

Fig. 16a-d show the scatter plots of droplet sizes. The experimental data is reported in the form of several radial measurements for a given droplet-size range. Unfortunately, the plots do not contain any information on the number density of a given particle group. Although the experimental data shows a wider presence radially, only some of the droplet groups do contain most of of the mass. The results show that the droplet sizes are well represented by both the PDF and non-PDF computations but the non-PDF computations show a far less number of droplets within the reported experimental range of the last location. In the non-PDF computations, the droplets traversing the central region of the jet vaporize more rapidly as they are exposed to temperatures of about 2100 K for a longer period of time. This would explain the reason for the lack of enough number droplets in this range.

12.2 A 3D Test Case

Here, the results of a 3D test case are summarized. Fig. 17 shows the geometry of the combustor configuration used in the computations. The inflow air flows through an annular opening of 45-degree swirl vanes with a flow speed of about 28.25 m/s and a mass flow rate of about 41.1 g/s. For the annular opening, the dimensions of the outer and inner radii are 3.2 and 1.5 cm, respectively. N-heptane fuel was injected in the form of single hollow cone stream with a mass flow rate of about 2.7 g/s. Solid wall boundary conditions were applied on the boundaries shown with the surface grids; the top and bottom surfaces as well as those on the frontal surface. The flow exits through the backward surface and periodic conditions were applied on the remaining left and right surfaces. Both the PDF and the non-PDF computations were performed for this case on a computational grid comprising of 8430 tetrahedral elements and 100 Monte Carlo PDF particles per cell.

The velocity vector plot of Fig. 18 shows the formation of a vortex swirling in the clock-wise direction near the inflow boundary. The flow becomes more unidirectional further downstream as it flows towards the exit boundary. Initially, most of the spray particles move towards the upper left corner near the top wall, and from there onwards, the particles seem to drift downstream towards the exit. This leads to a concentration of fuel vapor near that left location of the upper wall from the vaporizing droplets as shown in Fig. 20. The temperature contours of Fig. 19 show that a flame originating near the left corner of the top wall surface, propagates radially outwards as it moves downstream. The fuel and oxygen mass fractions of Figs. 20 and 21 confirm this observation as the fuel vapor from the vaporizing droplets near the upper wall mixes and burns with surrounding air to support a flame originating from that location.

13 CONCLUDING REMARKS

A solution procedure was developed for spray computations based on the scalar Monte Carlo PDF method for application with unstructured grids and parallel computing. The solution procedure seems to be able to capture the overall structure of a

Table 1. Cpu time (sec) per cycle versus number of PEs.

Solver	Characteristic	Number of processors		
		2	5	10
CFD	5 steps/cycle	2.50	1.25	0.75
PDF	1 step/cycle	6.5	2.9	1.9
Spray	100 steps/cycle	1.70	0.64	0.53

spray flame well, and its application to several spray flames (both confined as well as unconfined) showed reasonable agreement with the available spray measurements.[7,9]

The detailed comparisons made for the case of a reacting spray illustrated the importance of chemistry/turbulence interactions in the modeling of a reacting spray. The PDF results were found to be closer to the reported experimental data when compared with the non-PDF solution. The PDF computations predict that some of the combustion occurs in a predominantly premixed-flame environment and the rest in a predominantly diffusion-flame environment. However, the non-PDF solution predicts wrongly for the combustion to occur in a vaporization-controlled regime. Near the premixed flame, the Monte Carlo particle temperature distribution shows two distinct peaks: one centered around the flame temperature and the other around the surrounding-gas temperature. Near the diffusion flame, the Monte Carlo particle temperature distribution shows a single peak. In both cases, the PDF's shape and strength are found to vary substantially depending upon the proximity to the flame surface. The results cast some ambiquity regarding the applicability of the widely used assumed-shape PDF methods in spray computations.

The paper also demonstrated the results from a 3D test case which was designed primarily to demonstrate the computational viability of the Monte Carlo PDF method for 3D computations and also to examine the applicability of the spray particle search algorithm in 3D computations and of the newly-implemented periodic boundary conditions.

As mentioned in the previous section, the computations for the 3D test case were performed on a grid of 8,450 elements with a total of 0.845 million particles (=100 particles/cell). The computations were performed on one of the NASA Ames Research Center's parallel computer platforms called Turing which is a SGI Origin work-station with 24 PEs (Processor Elements). Table 1 summarizes the cpu times per cycle taken by the PDF, spray, and CFD solvers vs the number of PEs. All of the CFD, PDF and spray solvers show good parallel performance with an increase in the number of processors.

The additional computational burden associated with use of a Monte Carlo PDF method should be considered to be moderate in view of the the normal cpu times taken by the conventional single-processor CFD/spray solvers. The viability of the present method for its application to the modeling of practical combustion devices is demonstrated through the use of unstructured grids and the ability to run the computations on massively parallel computers.

14 ACKNOWLEDGEMENT

The research funding for this work was provided by NASA Glenn Research Center with Dr. N.-S. Liu acting as the technical monitor.

15 REFERENCES

1. C.T. Crowe, M.P. Sharma, and D.E. Stock, The Particle-Source-in Cell (PSI-CELL) Model for Gas-Droplet Flows, J. Fluids Eng., vol. 99, pp. 325, 1977.
2. Y. El Banhawy and J.H. Whitelaw, Calculation of the Flow Properties of a Confined Kerosene-Spray Flame, AIAA J., vol. 18, no. 12, pp. 1503-1510, 1980.
3. G.M. Faeth, Mixing, Transport, and Combustion in Sprays, Prog. Energy Combust. Sci., vol.13, pp. 293-345, 1987.
4. M.S. Raju and W.A. Sirignano, Multi-Component Spray Computations in a Modified Centerbody Combustor, Journal of

Propulsion and Power, vol. 6, no. 2, pp. 97-105, 1990.

5. M.S. Raju, AGNI-3D: A Computer Code for the Three-Dimensional Modeling of a Wankel Engine, Computers in Engine Technology: Proceedings IMechE, London, United Kingdom, pp. 27-37, 1991.
6. M.S. Raju, Heat Transfer and Performance Characteristics of a Dual-Ignition Wankel Engine, Journal of Engines - Section 3, SAE Trans., vol. 101, pp. 466-509, 1992.
7. M.S. Raju, Application of Scalar Monte Carlo Probability Density Function Method For Turbulent Spray Flames, Numerical Heat Transfer, Part A, vol. 30, pp. 753-777, 1996.
8. M.S. Raju, LSPRAY - A Lagrangian Spray Solver - User's Manual, NASA/CR-97-206240, NASA Lewis Research Center, Cleveland, Ohio, November 1997.
9. M.S. Raju, Combined Scalar Monte Carlo PDF/CFD Computations of Spray Flames on Unstructured Grids With Parallel Computing, AIAA/ASME/SAE/ASEE 33rd Joint Propulsion Conference, Seattle, Wash., July 6-9, 1997.
10. M.S. Raju, Current Status of the Use of Parallel Computing in Turbulent Reacting Flows: Computations Involving Sprays, Scalar Monte Carlo Probability Density Function & Unstructured Grids, Advances in Numerical Heat Transfer, vol. 2, ch. 8, To appear.
11. R. Borghi, Turbulent Combustion Modeling, Prog. Energy Combust. Sci., vol. 14, pp. 245-292, 1988.
12. S.B. Pope, PDF Methods for Turbulent Reactive Flows, Prg. Energy Combust. Sci., vol. 11, pp. 119-192, 1985.
13. D.B. Spalding, Mathematical Models of Turbulent Flames: A Review, Combustion Science and Technology, vol. 13, pp. 3-25, 1976.
14. S.M. Correa, Development and Assessment of Turbulence-Chemistry Models in Highly Strained Non-Premixed Flames, AFOSR/NA Contractor Report, 110 Duncan Avenue, Bolling AFB, DC 20332-0001, 31 October 1994.
15. H.M. Shang, Y.S. Chen, P. Liaw, M.H. Shih, and T.S. Wang, Numerical Modeling of Spray Combustion With an Unstructured-Grid Method, AIAA 95-2781, AIAA/ ASME/ SAE/ ASEE 31st Joint Propulsion Conference, San Diego, Calif., July 10-12, 1995.
16. R. Ryder, CORSAIR User's Manual: Version 1.0, SID: Y965, Pratt and Whitney Engineering, United Technologies Corporation, 25 January 1993.
17. N.S. Liu and R.M. Stubbs, Preview of National Combustion Code, AIAA 97-3114, AIAA/ASME/SAE/ASEE 33rd Joint Propulsion Conference, Seattle, Wash., July 6-9, 1997.
18. K.-H. Chen, A.T. Norris, A. Quealy, and N.-S. Liu, Benchmark Test Cases For the National Combustion Code, AIAA 98-3855, AIAA/ASME/SAE/ASEE 34th Joint Propulsion Conference, Cleveland, Ohio, July 13-15, 1998.
19. M.S. Raju, EUPDF - An Eulerian-Based Monte Carlo Probability Density Function (PDF) Solver - User's Manual, NASA/CR-1998-20401, NASA Lewis Research Center, Cleveland, Ohio, April, 1998.
20. V.G. McDonell and G.S. Samuelson, An Experimental Data Base for the Computational Fluid Dynamics of Reacting and Nonreacting Methanol Sprays, J. Fluids Engineering, vol. 117, pp.145-153, 1995.
21. W.A. Sirignano, Fluid Dynamics of Sprays, Journal of Fluids Engineering, vol. 115, no. 3, pp. 345-378, September 1993.
22. T.-H. Shih, K.-H. Chen, and N.-S. Liu, A Non-Linear $k - \epsilon$ Model for Turbulent Shear Flows, AIAA/ASME/SAE/ASEE 34th Joint Propulsion Conference, Cleveland, Ohio, July 13-15, 1998.
23. A.Y. Tong and W.A. Sirignano, Multicomponent Transient Droplet Vaporization With Internal Circulation: Integral Formulation and Approximate Solution, Numerical Heat Transfer, vol. 10, pp. 253-278, 1986.
24. R. Clift, J.R. Grace, and M.E. Weber, Bubbles, Drops, and Particles, Academic, New York, 1978.

25. H. Schlichting, Boundary-Layer Theory, McGraw-Hill Series in Mechanical Engineering: McGraw-Hill, Inc., New York, 1968.

26. F.V. Bracco, Modelling of Engine Sprays, SAE paper 850394, 1985.

27. M. Scheurlen, B. Noll, and S. Wittig, Application of Monte Carlo Simulation For Three-Dimensional Flows, AGARD-CP-510: CFD Techniques For Propulsion Applications, February 1992.

28. D.A. Anderson, J.C. Tannehill, and R.H. Fletcher, Computational Fluid Mechanics and Heat Transfer: Series in Computational Methods in Mechanics and Thermal Sciences, Hemisphere Publishing Corporation, Washington, D.C., 1984.

29. M.S. Raju, W.Q. Liu, and C.K. Law, A Formulation of Combined Forced and Free Convection Past Horizontal and Vertical Surfaces, Int. J. Heat and Mass Transfer, vol. 27, pp. 2215-2224, 1984.

30. C.K. Westbrook and F.L. Dryer, Chemical Kinetic Modelling of Hydrocarbon Combustion, Progress in Energy and Combustion Science, vol. 10, no. 1, pp. 1-57, 1984.

31. A.T. Hsu, Y.-L.P. Tsai, and M.S. Raju, A Probability Density Function Approach for Compressible Turbulent Reacting Flows, AIAA Journal, vol. 32, no. 7, pp. 1407-1415, 1994.

32. D.L. Bulzan, Velocity and Drop Size Measurements in a Confined, Swirl-Stabilized Combusting Spray, AIAA 96-3164, 32rd AIAA/ ASME/ SAE/ ASEE Joint Propulsion Conference, July 01-03, 1996/Buena Vista, FL.